POLITECNICO DI TORINO

Master's Degree in Aerospace Engineering

Master's Degree Thesis

Experimental and FEM Analysis of a new configuration of material for orbital uses

Supervisor

Prof. Giacomo FRULLA

Co-Supervisors

Dr. Ing. Nicola GIULIETTI

Candidate

Giuliana Carmela DEL VECCHIO S279422

03/2022

Summary

In recent years, spacecrafts have become increasingly important especially in the orbits LEO (Low Earth Orbit) and MEO (Medium Earth Orbit) as a result of increased missions (especially telecommunications). Consequently, the need for new, lighter and more reliable materials is also becoming a crucial point as a balance must be made between the various problems concerning the space environment (radiation, thermal effects, outgassing) and the urgency of lightening the structures while maintaining good properties. Among the materials that most meet the above requirements, as well as having good corrosion and impact resistance characteristics, there is the sandwich which consists mainly of three different layers (two layers usually composite and a central part foam). The following thesis work focuses on a new configuration of Madflex, a material developed by the company Composite Research that has as its main feature to be rollable on one side while on the other it has a rigid behavior, adaptable to the space environment. Consequently, the study of the material focuses on a first part of the verification of the flexural characteristics of the material, according to the ASTM D7250/D7250M standard and a comparison with the data derived from FEM analysis. Subsequently, it was considered appropriate to proceed with an ageing test of the material using gamma rays to test the change in mechanical characteristics when the material is subject to a long period of radiation exposure. Finally, a thermal analysis was carried out to see the behavior of the material under certain temperature conditions.

Table of Contents

List of Tables

List of Figures

Acronyms

CVCM
: Collected Volatile Coondensable Material

GCR
: Galactic Cosmic Rays

GEO
: Geostationary Earth Orbit

LEO
: Low Earth Orbit

MEO
: Medium Earth Orbit

RML
: Recovered Mass Loss

SAA
: South Atlantic Anomaly

SEE
: Single-Event Effect

TID
: Total Ionising Dose

TML
: Total Mass Loss

TPS

Thermal Protection System

UHTM

Ultra-high Temperature Material

Chapter 1

Space environment in low earth orbit

The space environment represents a continuous challenge for materials and structures due to the difficulties associated with the operating conditions. In fact, Spacecraft are subject, from low earth orbit to deep space, to a series of problems leading to numerous consequences such as material degradation, contamination, radiation damage and interferences. In recent years, there has been a growing interest in this sector, especially in the field of scientific research, which has led to the definition of regulations and requirements necessary for operating in the various space orbits. Furthermore, although the space environment is complex and risky, there is a growing demand for lighter structures [1], which leads to the use of more and more special materials. An attempt is therefore made to balance the risk associated with the operation against the costs involved. In general, in order to define a new space technology, the following steps are taken:

- definition of spatial conditions and operating environment
- definitions of mission requirements and the main critical effects that can affect structures
- definition of project performance and design
- definition of mission risk and main margins
- iteration of the process

In general, we can make a classification of the spatial environment as a function of altitude, as shown in Table 1.1. The space environment can, therefore, present differences depending on the proximity to the sun, to the Earth and other effects that will be described below.

Orbit	Altitude
LEO (Low Earth Orbit)	<10,000 Km
GEO (Geostationary Orbit)	<35786 Km
MEO (Medium Earth Orbit)	<15 000 Km

Table 1.1: Different orbits and relative altitudes

1.1 The solar effect

The sun is a medium-small star [1], composed of a nucleus formed by hydrogen (approximately 74% of its mass, 92.1% of its volume) and helium (approximately 24-25% by mass, 7.8% by volume). Currently it is in a stable equilibrium phase in which a continuous fusion takes place within the nucleus that generates, in the unit of time, a large amount of energy in the form of radiation. The space environment is strongly influenced by these phenomena (gamma radiation, x-rays, plasma, high-energy particles), which vary in time depending on the solar cycle. Moreover, these events can hardly ever be assessed with certainty, but statistical analyses must be carried out. Another main effect to be considered is the strong variability of its magnetic field (Fig.1.1)in both the short (short duration storms) and long term. This effect causes strong variations within the space environment that must be taken into account. The solar corona emits a continuous stream of

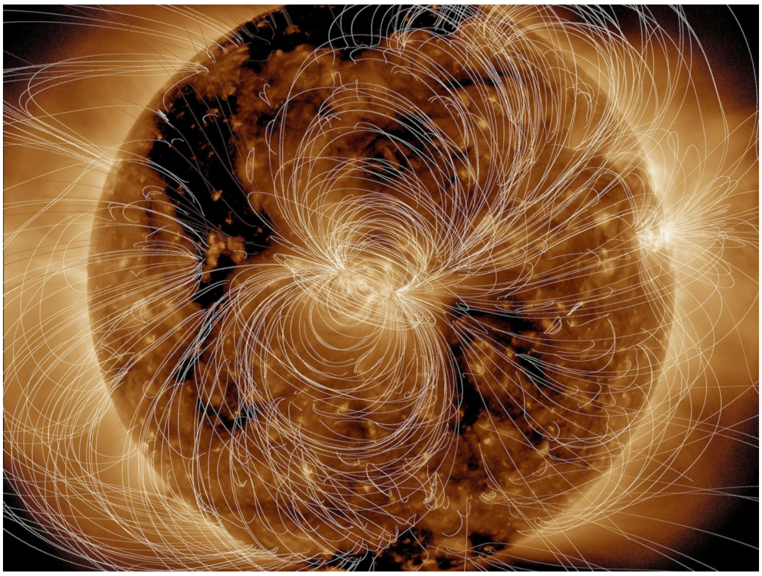

Figure 1.1: solar magnetic field

electrons and protons and ions that form the so-called solar wind, which, according to recent research [2] extends up to 17 billion kilometres from Earth. The energy of the particles varies from about 0.5 to 2.0 keV/n while the density of the solar wind is about 1 to 30 $particles/cm^3$. In addition, temperatures around the sun reach high values and, as a consequence of this, electrons escape from the sun's gravitational field causing a charge imbalance that leads to an ejection of heavier ions and protons. The gas is mainly composed of plasma, as the temperature is so high that an amalgamation of the particles takes place. The table 1.2 shows the main particles that make up the solar wind:

Particle	Quantity
Protons	96 %
Alpha Particle	4 %
Ions	<1 permille

Table 1.2: main components solar wind

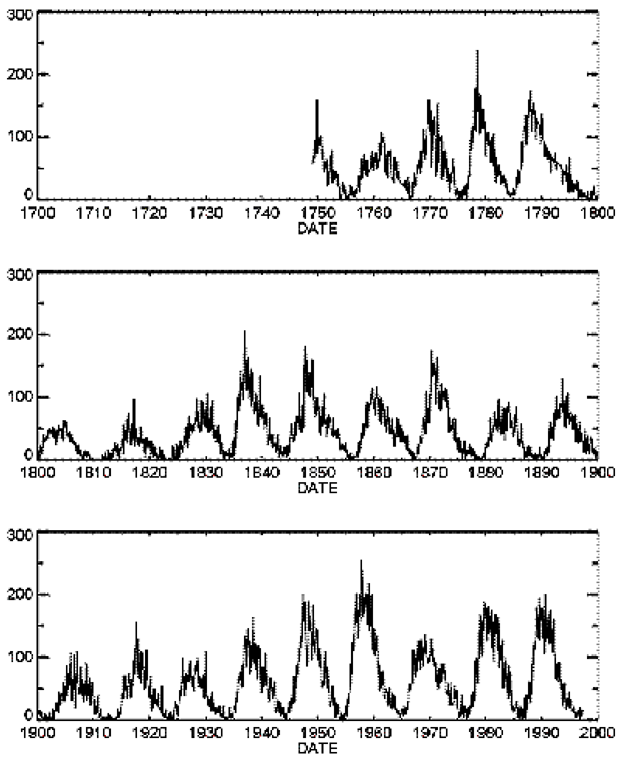

Figure 1.2: Solar cycles

The sun's activity, as mentioned above, varies according to solar cycles (Fig 1.2). Sunspots appear cyclically on the sun's surface, and when the number is high, the sun's activity is more intense, causing a greater emission of radiation into the surrounding space. The average solar cycle lasts 11 years, but it can also vary between 10 and 12 years [2]. Solar cycles, in addition to the various characteristics described above, also have the function of modulating certain phenomena occurring in space. In fact, both Galactic comic rays (GCR) and atmospheric neutrons (resulting from the collision between GCRs and the Earth's atmosphere) are conditioned by solar cycles. Also, particles trapped in the magnetosphere are affected by solar activity levels. In addition to the solar wind, two other major factors related to the sun must be considered, namely solar flares (Fig 1.3)and coronal mass ejections (Fig. 1.4). A flare [3] is a strong eruption of matter that releases a high amount of energy. The radiation associated with this level of energy can cause various types of damage, especially to spacecraft located outside the Earth's magnetosphere. A flare can be classified into five different categories [3] according to its brightness in x-rays (A, B, C, M, X).Coronal mass ejections, on the other hand, consist of the ejection of a large amount of plasma into interplanetary space. These usually occur when the magnetic field assumes an 'arc' configuration and traps a plasma bubble. This bubble becomes unstable, causing the plasma to escape and, via the solar wind, be blown towards interplanetary space. Typically, the amount of plasma that can be released during the entire process is $10^{1}7$grams of plasma at a speed of 200 to 2000 km/s [3].

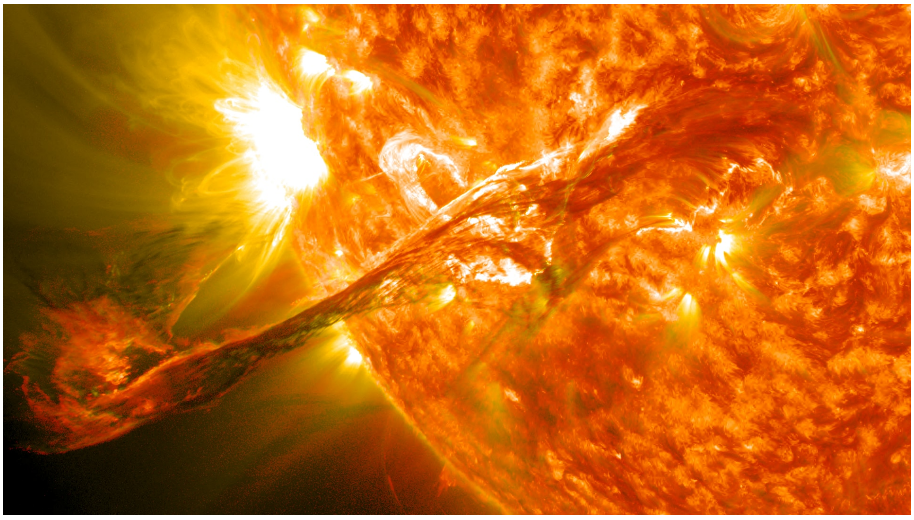

Figure 1.3: solar flares

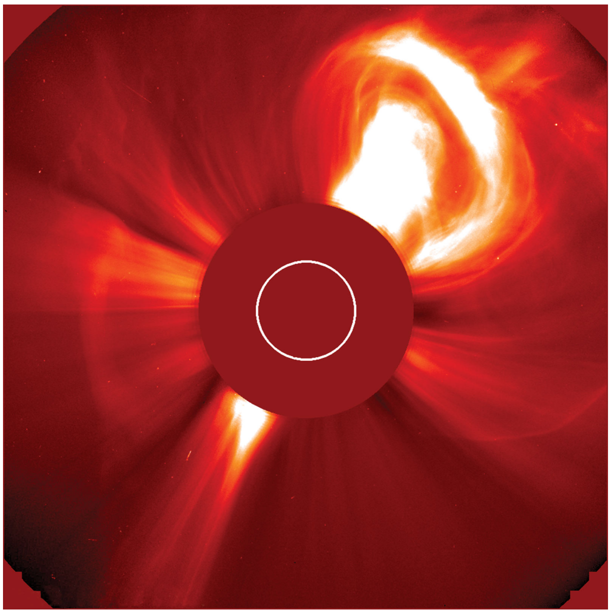

Figure 1.4: coronal mass ejections

1.2 Ultraviolet Radiation

The sun is the main source of ultraviolet radiation covering a wavelength of between 100 and 400 nanometres [4]. If we consider the solar constant about 9 % of this is in the ultraviolet. The intensity of ultraviolet radiation depends on several factors, such as the ellipticity of the Earth. In fact, between aphelion and perihelion there is a variation in the Sun-Earth distance of about 3% [4] and this can cause a variation in UV levels. In addition, the radiation is diffused by a constant that is inversely proportional to the radial distance from the sun. Knowing the level of radiation is important because UV rays, interacting with atoms in the atmosphere (especially oxygen), cause degradation of the spacecraft surface.

1.3 Plasma

Plasma is a state of matter in which, as a result of the high temperatures of celestial bodies, atoms are ionised. Inside the plasma there is approximately the same density of electrons and protons and the energy is <100keV [1]. The main sources of plasma include the ionosphere, which is characterised by low energy and high density. Other sources are geomagnetic sub-storm activity and the solar wind.

1.4 Orbital Debris and Meteoroids

Space debris is a problem that has been gaining in importance in recent years as it is closely linked to the safety of spacecraft and it includes both meteorites and any debris resulting from human action. The main phenomena (Fig 1.5) that can lead to the formation of debris include [5]:

- decommissioned satellites at the end of their lifecycle;
- satellite debris resulting from accidents;
- engine exhaust products;
- detritus released during the course of the mission;

In order to be able to assess the probability of impact and especially the effect this could have on the aircraft, experimental tests and empirical analyses were carried out [5]. From these it was discovered that collisions leading to complete fragmentation of the target are those for which the energy ratio is greater than a given value:

$$\frac{0{,}5 E_{impactor} V_{impactor}^2}{E_{target}} \geq 40 \frac{J}{g} \tag{1.1}$$

Micrometeorites and debris can cause numerous problems for spacecraft as they

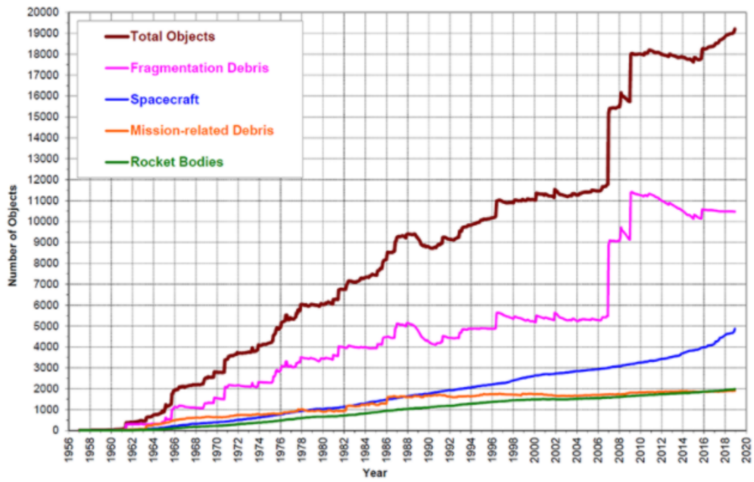

Figure 1.5: Number of objct in Low Eart Orbit

can cause structural damage and decompression or surface damage such as erosion that can also lead to changes in the physical, mechanical or thermal characteristics of the structures themselves.

1.5 Earth's atmosphere

The Earth's atmosphere consists mainly of molecular nitrogen (about 78%) and molecular oxygen (about 21%) [6]. In addition to the gases mentioned above, which are mainly present in the atmosphere, there are others such as argon (less than 1%), carbon dioxide (increasing, but currently present at 0.0390%) and finally methane (0.00018%). Both the sun and other planets, unlike the Earth, also have hydrogen and helium, but these are not present within the Earth's atmosphere because the gravitational field is weak and temperatures are greatly reduced. The Earth's atmosphere, unlike many other planets, has a high proportion of oxygen, which combines with many chemicals due to its high reactivity [6]. This latter phenomenon has both positive consequences for the planet and for spacecraft, and negative consequences, especially in terms of erosion of structures. The Earth's atmosphere is commonly divided into several layers and has a constant composition up to about 100 km [1]. The first layer is the Troposphere (About 0-15 Km) where there is a temperature gradient of about 6°C per km (Fig. 1.6). Beyond the troposphere is a layer called the stratosphere (About 15-50 Km), the latter of which shows an increase in temperature with altitude. The Mesosphere (About 50-80 Km), present beyond the stratosphere, is affected by a decrease in temperature and a minimum variation depending on the season.

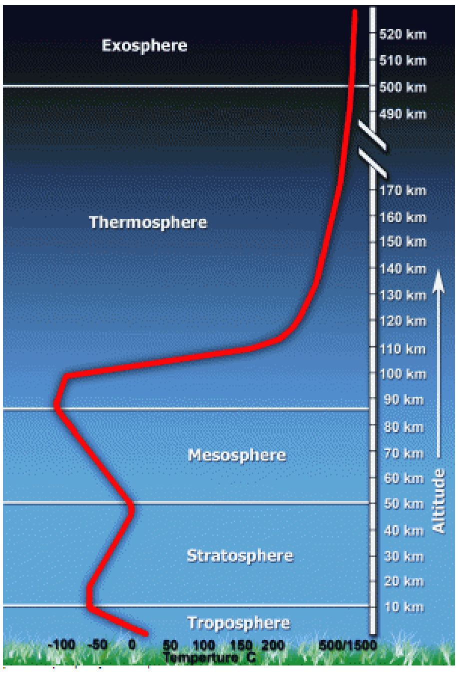

Figure 1.6: temperature variation in the various layers of the atmosphere

Beyond the Mesosphere lies the Thermosphere (about 80-600 Km) where again temperatures tend to increase. This layer is mainly composed of neutral gases, in fact the lower thermosphere has a higher percentage of atomic oxygen [1], hydrogen and helium than the upper thermosphere. In these layers, as a result of the absorption of extreme ultraviolet radiation, heating causes a change in the distribution of neutral gases. The latter tend to degrade the surface of the materials and cause the glow on the spacecraft [1] (generated by the excitation of metastable molecules) as well as causing a change in the mechanical, physical, thermal and optical characteristics of the material [6]. In addition, there is drag, a function of gas density and solar activity, which leads to spacecraft decay. Lastly is the Ionosphere mainly composed of low-energy, high-density plasma. In recent years, a great deal of research has been carried out on this layer, aimed at improving satellite communications, which are severely damaged by large-scale storms affecting radio waves. In addition, there are special phenomena within the ionosphere that cause not only damage to communication, but also the coupling effects of the solar array with the plasma that causes a current drain on the solar arrays [1]. In conclusion, the Earth's atmosphere has quite significant internal variations in its attributes with consequences for the characteristics of materials.

1.6 Magnetosphere

The Sun, at every instant of time, emits high-energy particles that travel through space at high speeds. These are deflected by the Earth's magnetic field, or magnetosphere, generated by the rotation of the iron core at the centre of the planet. It extends for about 25000 km [7], for its shadowed part, while during the day, under the pressure of the solar wind, it can reach 60000 km [7]. Its shape derives precisely from iteration with the solar wind, without which it would have the shape of a bar magnet (a representation considered accurate to about 5 Earth degrees). Plasma interacting with the magnetosphere tends to compress it, generating the so-called 'bow shock' through which the solar wind plasma cannot pass due to its charged particle composition. As a result, about 99.9% of these particles are forced to pass around the Earth's magnetosphere, creating its characteristic shape [7]. Fig. 1.7 shows some characteristic areas of the magnetosphere such as the plasma sheet embedded in the tail, or the Van Allen belts located above the plasmasphere. In addition, the particles remain stationary within the magnetic field as they are confined by the magnetic field and are forced to rotate in a helical path, bouncing from one pole to another.

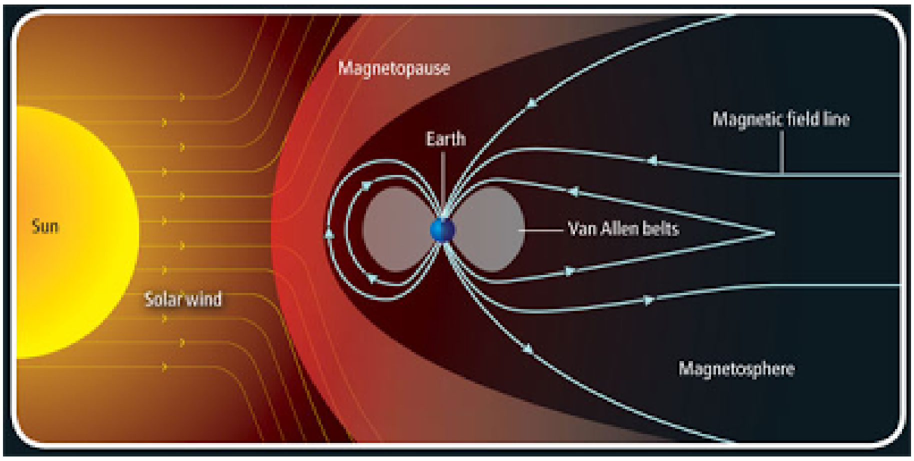

Figure 1.7: Earth's magnetosphere

One of the effects and complications arising from the magnetosphere, which mainly affect missions in GEO, GTO and MEO orbits, are the so-called "hot plasmas" that are created by geomagnetic substorms located in the plasma layer inside the tail. One of the main problems associated with this phenomenon is that electronic instruments can be distorted, disturbed, attract contaminants and finally sputtering can cause increased erosion of the material. Another phenomenon to be considered are the Van Allen Belts (Fig. 1.8), in which electrons (possessing energies up to 10 MeV), protons and heavy ions (up to 100 MeV) are trapped on magnetic field lines [1]. Within the Van Allen belts, the particles are positioned in a complex way depending on the altitude and inclination of the orbit as well as solar activity. Particles within the belts are severely damaging to spacecraft. The South Atlantic Anomaly (SAA) [1] is one of several anomalies that are most likely to affect satellites in low Earth orbit. In this particular condition, particles are stranded at low altitude because there is a depression of the magnetic field in the South Atlantic caused by an 11° inclination between the magnetic and geographic axes and the distance between the magnetic and geometric centres. The main effects are listed below:

- **Total Ionising Dose (TID)** or **displacement damage**:This phenomenon is mainly caused by the exposure of spacecraft to particles which, on coming into contact with the material, tend to stop and blow out atoms causing a distortion of the crystal structure and a consequent creation of defects. TID is a cumulative effect that can lead to the degradation, and relative disuse, of various instruments such as solar cells, and energy spectra are used to capture the level of radiation;

- **single-event effects (SEE)**: these effects are related to the iteration of the single particle with particular areas of the electronic device, and can be single-event upsets, single-event latchups and single-event transients.

- **deep dielectric charge**: high-energy electrons enter dielectric materials and discharge, causing damage to circuits and materials;

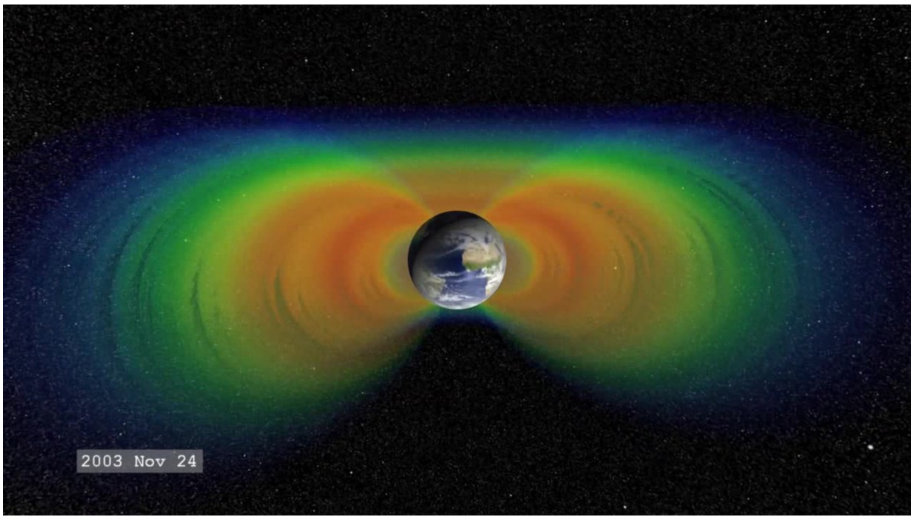

Figure 1.8: Van Allen Belts

1.7 Galactic Cosmic Rays

One of the main hazards affecting spacecraft operating outside the magnetosphere is the nuclei of Galactic Cosmic Rays. The main factors that can lead to dangerous effects on structures are listed below [8]:

- shielding effects;
- effect of spatial and temporal variation of Galactic Cosmic Ray nuclei;
- effects related to the energy spectra of nuclei;
- the so-called "stopping power";

Once the various risk factors have been defined, it is possible to analyse the composition of galactic cosmic rays, as well as the energy associated with the spectrum of nuclei. First of all, it must be considered that Galactic Cosmic Rays, after about 45 years of study and research related to the phenomenon, are composed essentially of all the elements of the periodic table [8]. (nuclear charge variant 1 to

92). In particular, considering a first approximation, they are composed of main elements whose abundances and distributions are similar to those present both on the sun and on meteorites, but in reality the Cosmic Galactic Rays include within them a high quantity of secondary nuclei produced as a consequence of the crumbling of heavier nuclei [8]. They also have an overabundance of H and He and a lower presence of elements with high first ionisation potential. In order to analyze the energy of the Galactic Cosmic Rays it is possible to draw a graph representing the kinetic energy per nucleon (Fig 1.9), from which it is noted that all the nuclei have a spectral form very similar to each other. In particular it can be observed that the law of the secondary species decays with a higher speed than the energies of the most abundant species, moreover below a certain value equal to 1GeV/nuc there are the so-called effects of "solar modulation" where curve flattening occurs. Even if it is not strictly visible from the diagram, it has been

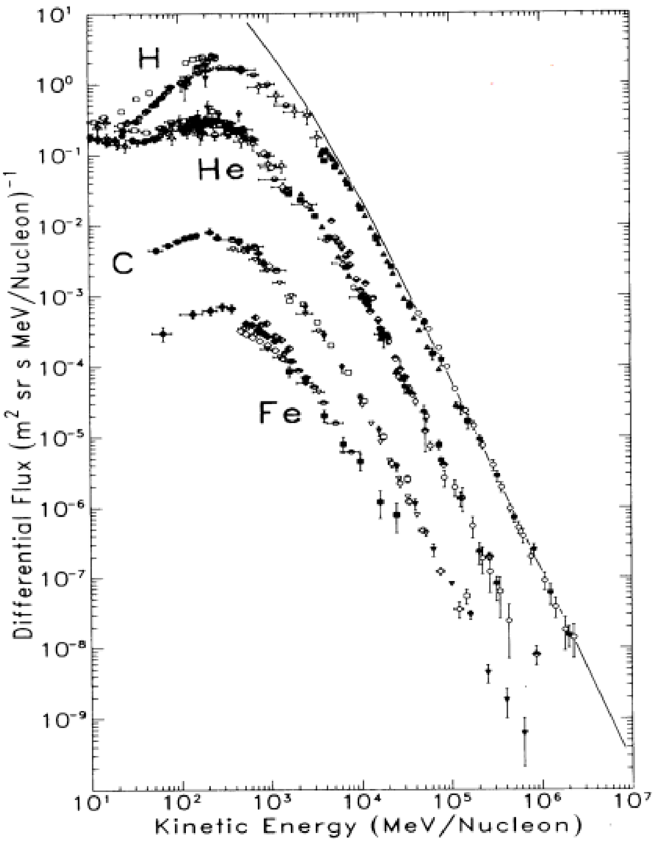

Figure 1.9: Cosmic Ray Energy spectra for the elements H, He, C, and Fe

realized that there are important variations of the composition of the nuclei in function of the energy, in fact the secondary nuclei have a greater quantity from approximately 1 to 2 Gev/nuc. Finally it can be summarized that the composition of the Galactic Cosmic Rays includes a percentage equal to 98% of H, He, C, O, Ne, Mg, Si, S, Ca and Fe and through an integration of energy spectra it is noted that more than 75% of particles have a kinetic energy of less than about 2 Gev/nuc [1]. Galactic cosmic rays represent a reduced danger at the solar peak, although the probability of large solar particle events is increased. For periods of minimal solar activity, essential to assess the risk, there has been a significant change over the years in terms of both duration and energy. After various researches it has been realized that the cycle of final modulation of the sun has a period of about 22 years and not 11 due mainly to the transport of the Cosmic Rays in the heliosphere and to their dependence with the polarity of the solar magnetic field [1].

1.8 Comparison with other Planets

In addition to the Earth's atmosphere, it is also useful to have a vision and a comparison with other planets in the solar system in order to better evaluate the requirements and the related mission assessments. In general, the planets have an atmosphere when the average molecular velocity of the gases present is considerably lower than the escape velocity and, within the solar system, Venus, Mars, Jupiter, Saturn, Uranus and Neptune have this characteristic [9]. Starting with Venus (Fig 1.10), the latter has about 96% carbon dioxide and temperatures are around 737 K [9]. In addition, Venus has a rotation of 243 days and can reach very high surface

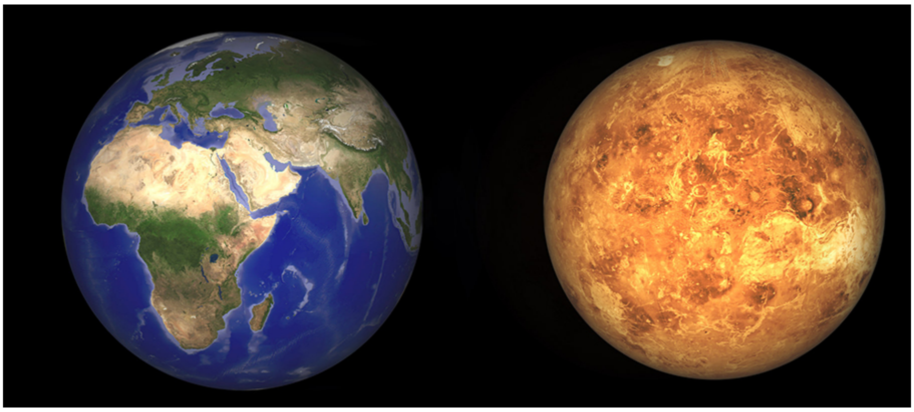

Figure 1.10: Comparison between Venus and Earth

pressures (95,000 millibars). Mars (95% carbon dioxide and a remaining part of diatomic nitrogen) has a surface temperature of about 210K with a pressure very close to 6 millibars [9]. In addition, periodic storms are observed on the planet (due to the intersection of cold air from the polar ice cap and hot air from average altitudes) as well as clouds of water and carbon dioxide. The characteristic that unites mainly both Earth, Mars and Venus, is that the atmospheres were formed following volcanic eruptions with successive different evolutions in the three planets. On Venus, given the proximity to the sun, there was a dissolution of water in oxygen (recombinated with other elements) and hydrogen gas (lost in space), while on Mars, given the low temperature, water vapor was deposited, in the form of ice, inside the crustal soils [9]. The atmosphere of Jupiter and Saturn is formed by hydrogen and helium with small percentages of methane. Both planets are characterized by the circulation of clouds and regional phenomena at certain speeds creating very turbulent vortices. Finally, it is possible to mention Uranus and Neptune which have characteristics very similar to those of Jupiter and Saturn. In the table are inserted the main components of the atmosphere of the various planets[9]. The atmosphere of Jupiter and Saturn is formed by hydrogen and helium with small percentages of methane. Both planets are characterized by the circulation of clouds and regional phenomena at certain speeds creating very turbulent vortices. Finally, it is possible to mention Uranus and Neptune which have characteristics very similar to those of Jupiter and Saturn. In the tables 1.3 and 1.4 are inserted the main components of the atmosphere of the various planets.

	Percentage	Gas
Mercury	42 %	O_2
	29 %	Na
	22 %	H_2
	7 %	Others
Venus	96 %	CO_2
	3 %	N_2
	1 %	Others
Mars	95 %	CO_2
	3 %	N_2
	1,5 %	Ar
	0,5%	Others

Table 1.3: Solar system planets atmosphere similar to Earth

	Percentage	Gas
Jupiter	90 %	H_2
	10 %	He
	1 %	Others
Saturn	96 %	H_2
	3 %	He
	1 %	Others
Uranus	83 %	H_2
	15 %	He
	2.5 %	CH_4
Neptune	80 %	H_2
	19 %	He
	1 %	CH_4

Table 1.4: Atmosphere solar system planets other than Earth

Analyzing, instead, more in detail the magnetic field of the other planets it can be noticed that the condition for the existence of a band of planetary radiation is that the magnetic moment must be large enough to make the solar flow stop [1]. The magnetic fields of the planets are similar to each other but the contribution of force varies (Fig 1.11). Neither Venus nor Mars have a magnetic field, although the

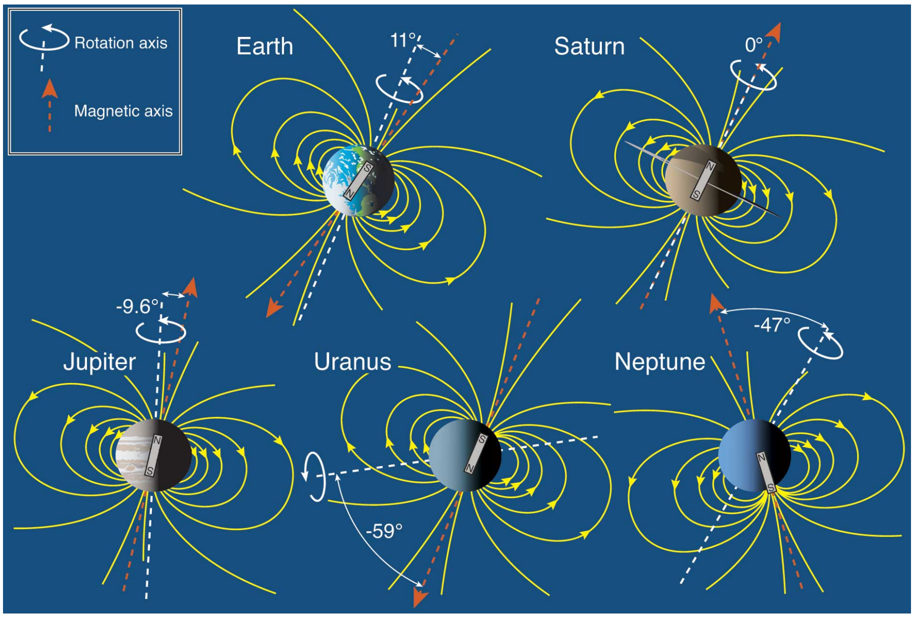

Figure 1.11: Magnetic Field of the Planets of the Solar System

Probos probe has revealed that Mars has a radiative environment. The latter is due, however, to the subtle atmosphere of Mars that allows the particles to penetrate the surface and the latter, interacting with the atmosphere, produce neutrons [1]. Jupiter, on the other hand, has a much higher magnetic field intensity than the Earth, in fact, as shown by the measurements, the radiative environment is much more intense than the terrestrial one. Finally, Saturn, Uranus and Neptune have magnetic fields very similar to Earth and whose intensity is considerably lower, which is why they are not a particular problem for spacecraft.

Chapter 2

Effects of space on materials

Once the operating conditions have been introduced, it is appropriate to define all the main problems that materials might encounter in space:

- **Temperature**: The solar radiation, the heat generated inside the satellite itself can lead to the heating of the material and the respective variation of the main characteristics;

- **High Vacuum**: the main problems are related to evaporation and sublimation of materials. The chemical atmosphere, resulting from the phenomenon of outgassing, leads to corrosive effects on materials as well as electrical arc-over or corona discharge;

- **Meteorites and micrometeorites**: They vary depending on the impact force, in fact larger clashes can cause variation in the shape of the component;

- **Shock**: no problems on materials, except impact with micrometeorites;

- **Vibration**: Except for the moment of launch, there are no particular issues;

- **X rays and gamma rays**:the iteration between the x-rays and the gamma is the material can cause its ionization causing displacement of the atoms and the subsequent variation of the chemical composition;

- **Magnetic fields and Gravitational fields**: there are no special effects on materials;

- **electrons and protons in Van Allen Belt**: also in this case the particles, trapped inside the Van Allen belts, can cause variation of the internal composition of the material;

- **Biological organisms**: the contamination can come from various space environments and, to prevent it, the aircraft are suitably sterilized (International Agreement);

2.1 Atomic oxygen

Atomic oxygen is formed by the dissociation of diatomic oxygen as a result of its exposure with ultraviolet radiation in an environment where it is impossible for it to recombine (in a environment with low density which varies according to the change in altitude Fig. 2.2). The first studies on atomic oxygen, carried out after the first flights of the Shuttle [10], had shown a modification of the exposed surfaces that had led to a substantial modification of the characteristics. In fact, undesirable temperature variations were observed which led to a decrease in the life of the component.
Another visible effect of atomic oxygen, moreover, is a brighter surface than before launch, an effect analyzed through post-flight research on painted surfaces.
The average velocity of the atomic oxygen flow is about 1.15 km/s [10] (the collision energy is about 4-5 eV) [10] while that of an aircraft can reach about 7.24 km/s [10] as a result, a collision takes place between atomic oxygen and the material that produces material erosion and contamination (Fig. 2.1).
Usually, in order to quantify the iteration between atomic oxygen and materials, the exposure time is evaluated and multiplied by the intensity of the atomic flow. Also can be calculated the probability that atomic oxygen, coming into contact with a material, reacts and this is identified as the probability of reaction. On the

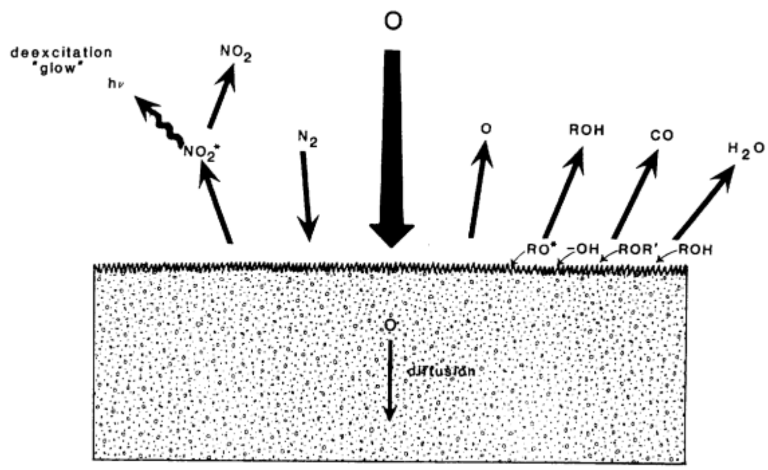

Figure 2.1: Change in atomic oxygen flow as a function of altitude

surface of the material subject to atomic oxygen, volatile oxides can form from polymers, or from carbon, or oxides can be created that tend to spall. These types of elements in any case produce surface erosion. As a result, the oxide forms on the

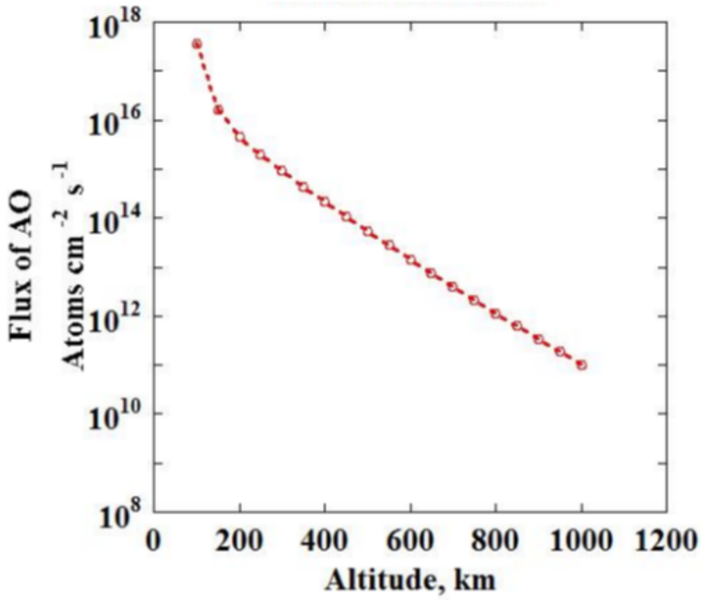

Figure 2.2: Change in atomic oxygen flow as a function of altitude

surface layer while the remaining part is analysed and the existence of a significant erosion of the surface is verified.
As mentioned above, it is possible to evaluate the probability of reaction of a given material in contact with atomic oxygen, and this type of operation can be carried out in case the materials form simple oxides.
Tests carried out in space [11] showed that in the case of Silver (unlike carbon, which has a probability of reaction of 13 % [11]) the probability of silver oxide formation is very high and is about 65 % [11].
For polymers, however, there are various mechanisms that can take over in the case of contact with atomic oxygen.

- **abstraction**: in this case the atom is extracted from the atomic oxygen from the material (hydrogen is usually extracted from saturated organic molecules from ground state atomic oxygen O(3p));
- **Insertion**: in this case the atomic oxygen interposes between two bound atoms (insertion within C-H bond of an atom of atomic oxygen that lead to the formation of alcohols);
- **Addition**: atomic oxygen, in this particular mechanism, aggregates to the

material;

- **Substitution**: atomic oxygen aggregates to a molecule leading to the removal of a part of it (alkyl radicals and radical alkoxys);

Specifically, atomic oxygen (both in graphite and polymers) tends to create microscopic superficial structures (tending to be conical) that increase in the prismatic plane. In the case of bombardment of the basal plane of graphite (Fig.2.3), even if there are no specific causes of its development, a layer of superficial texture [11] is also formed.
Finally, it has been noted experimentally that, due to the presence of the epoxy matrix, epoxy carbon fiber composites tend to erode more easily in contact with atomic oxygen due to the presence of the resin.
PAN fibres, on the other hand, develop a conical surface characteristic following the attack. In general, this can be applied to all bulk products with a volatile oxidation component that tend to develop surfaces that behave microscopically like the PAN.
Following an experiment conducted by Gregory in space on STS-8 [11] it was noticed that, the part of atomic oxygen that does not react with the surface state disperses off the surface, or may lie on it. Another parameter that greatly affects

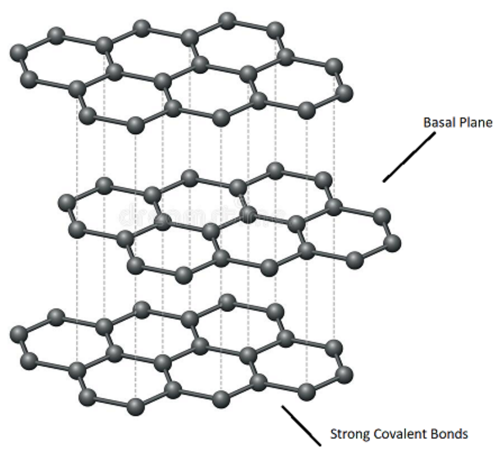

Figure 2.3: Graphite structure

the rate of erosion is the impact angle of atomic oxygen, in fact the variation of erosion varies in proportion to the cosine of the angle compared to the normal at the surface, as a result, it can be seen that highly inclined surfaces have a greater dispersion than atomic oxygen.
In addition, the erosion of atomic oxygen depends on both the activation energy

and temperature, as shown in the following formula:

$$Erosion - yield \propto e^{-}\frac{\Delta E}{RT} \tag{2.1}$$

It is also possible to observe, as a result of experimental research carried out [11], that the ratio between the level of erosion during the day and that during the night is very close to 1, as a result, there are no particular variations due to solar radiation.
However, in the researches [11] , the data showed a considerable dispersion therefore it is not possible to draw certain conclusions about the influence that the solar radiation can have.
In order to reduce the effect of atomic oxygen on structures, advanced thermoplastic materials and composites are used (although carbon-based materials degrade rapidly when they come into contact with these phenomena),
However, as can be seen from the table 2.1 [12],[13] some materials have very high rates of erosion, so that, sometimes, protective layers are provided, usually composed of metal oxide or thin metal films which, when properly applied, reduce the effect of atomic oxygen on the underlying layers. In general, the quality of a given coating depends on many factors, including the surface finish which must be as adequate as possible to reduce the infiltration of atomic oxygen to the underlying layers. As a result, some materials, such as graphite epoxy composites, which have rough surfaces, need suitable surface levelling coating systems [13].

Material	Erosion yield x $10^{-24} cm^{-3} atom^{-1}$
Diamond	0,021
Epoxy	1,7
Gold	0,0
Silicone	0,05
Aluminium	0,00
Carbon	1,2
Kapton	3
Polymide	3,0
Polypropylene	4,4
Pyrone	2,5
Siloxane polymide (7% Sx)	0,6
Polyethylene	3,3
Grafite epoxy	2,6

Table 2.1: Erosion yield of materials

In order to verify the ability of a coating to protect the material, it may be useful to assess, depending on the intensity of the atomic flow and the exposure time, the coating's ability to resist. For the calculation, therefore, the material is invested by atomic oxygen and decreases in weight are measured at different time intervals, from which it is possible to evaluate the effect F ($[atoms * cm^{-2}]$) [13] as :

$$F = \frac{M}{A\rho E} \tag{2.2}$$

where M is the mass loss in grams, A is the surface sample area in cm^2, ρ is density and E is the erosion yield expressed in $cm^3 atom^{-t}$.

2.2 Outgassing

Recently the space industry and especially the materials associated with it are presenting remarkable developments compared to the past and, in recent years, the focus on polymeric materials is growing [14].
Among the harmful effects that the materials have to endure is the outgassing that, causing the loss of the material, reduces the mechanical characteristics of the component itself.
Research in recent years has made progress in solving this problem, but no real solution has yet been found.
In fact, any material placed in a vacuum environment will tend to lose part of its mass.
In addition, after the polymerization process the polymers have a fairly high number of low molecular weight additives that will tend to spread to the surface and evaporate. The rate at which this last phase occurs is closely related to saturated vapour pressure (in fact, polymers for space applications usually contain a low vapour pressure value).
Outgassing can also impact not only materials, but also optical devices, and usually comes in the form of brown spots (Fig. 2.4) (on a generic aluminum panel).

Figure 2.4: Effect of outgassing on aluminium

As mentioned above the phenomenon of outgassing is quite problematic, in fact in the course of history there have been several cases related to it. Among these, for example, is the first lunar flight of Apollo 8 in which the silicone rubber seals have undergone outgassing leading to contamination of a large observation window [14]. Another case is the degradation of the CCD detector inside the NASA navigation sensor, or even the contamination of the camera on the Cassini probe [14]. In order to identify the effect that outgassing has on materials, it is possible to refer to the model proposed by Baeiss, which means that the change in outgassing is related to the mass of the remaining material and to a coefficient k depending on temperature.

$$\frac{dm}{dt} = -km \tag{2.3}$$

where it is possible to schematize k and m in the following way:

$$k = k_o e^{-\frac{E_a}{RT}} \tag{2.4}$$

$$m = m_o e^{-kt} \tag{2.5}$$

Recently, however, studies [14] have shown that the formulation used only adapts to the initial stage of outgassing, This is why, for the following phases, a diffusion process is implemented in order to better identify the variation of the phenomenon in the medium-long term. In a linear diffusion problem the characteristic equation is described by the following formula:

$$\frac{\partial C}{\partial t} = D\frac{\partial^2 C}{\partial x^2} + f(x,t) \tag{2.6}$$

Where it is possible to note the coefficients C and D, respectively equal to the concentration of the volatile part of the materials and the diffusion coefficient.as a result, the change in outgassing can be expressed as:

$$q = -D\frac{\partial C}{\partial x}|_{x=\delta} \tag{2.7}$$

Integrating results in the final amount of outgassing over a given period of time.

$$Q(t) = \int_0^t q(\tau)\, d\tau \tag{2.8}$$

With the following boundary conditions:

$$\begin{cases} C|_{x=0} = C|_{x=\delta} = 0 \\ C|_{t=0} = \varphi(x) \end{cases} \tag{2.9}$$

The solution of the problem will have a parabolic trend, moreover it can be solved with certainty only if the initial conditions are identified. Finally, it can be noted that the theoretical analysis described above does not take into account the internal effects of a spacecraft (such as internal pressure conditions).
In order to identify the influence that outgassing has on space materials, the "Mass-loss or weight-loss" method was commonly used [15]. This method consisted in suspending the sample on a very sensitive balance in a vacuum (10 -5 torr). The test consisted, therefore, of the continuous monitoring of the weight loss of the piece. The apparatus that was commonly used for this purpose was described by Podlaseck who implemented an Ainsworth scale (Fig. 2.5). A similar method was also used by Fulk and Horr.

To date, the test is certified according to ECSS-Q-ST-70-02C, which provides

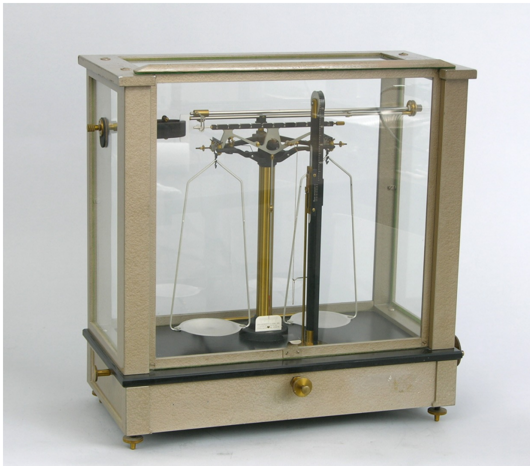

Figure 2.5: First Ainsworth balance of history

several steps and aims to identify the following fundamental parameters [16]:

- **TML (total mass loss)**: total mass loss relative to the initial sample mass;
- **RML (recovered mass loss)**: mass loss after water absorption during post-conditioning;
- **CVCM (Collected Volatile Condensable Material)**: collector mass gain over initial sample mass;

First the samples are placed in a preconditioning condition in order to be able to absorb moisture, Subsequently, the degassing behaviour during the thermal test is evaluated by measuring the sample weight before and after the process. The degree of contamination of the system and the mass gain of the collection plates are also measured.

In the table 2.2 are inserted the values of TML, RML and CVCM of some materials extracted from the database provided by NASA [17]:

Material	TML	CVCM	WVR
EPOXY FILM ADHESIVE GREEN	0,98	0,04	0,23
POLYURETHANE	0,44	0,07	
WHITE EPOXY FOAM	1,17	0,36	0,37
EPOXY LAMINATING FILM	0,31	0,09	0
CERAMIC ADHESIVE	2,7	0,02	0,57
SILICONE	1,08	0,51	0,02
POLYESTER	3,68	0,44	0,11
ALUMINA FILL EPOXY PASTE ADHESIVE	0,71	0,19	0,20
SILICONE	1,72	0,55	
SILVER FILLED SILICONE	0,60	0,21	
POLYETHYLENE	0,46	0,15	0
581 FABRIC	0,01	0	
CRP POLYPROPYLENE	0,53	0,33	0
FIBERGLASS WOVEN	0,23	0,03	0
POLYIMIDE FILM	1,04	0,01	1
GRAY SILICONE SHEET	1,56	0,46	0,02
TEFLON COATED FIBERGLASS FILM	0,02	0	0
TEFLON CARBON COATED TEFLON	0,53	0,01	0,47
TEFLON COATED KEVLAR	0,36	0	0,30
THERMOBOND SILICONE THERMAL CONDUCTIVE WHITE	1,62	0,32	0,07
POLYURETHANE FOAM	1,32	0	0,58
FOAM RIGID	1,88	0,01	1,15
POLYETHER-URETHANE FOAM	3,05	0,71	
IVORY URETHANE FOAM	1,09	0,02	0,20
POLYURETHANE FOAM OPEN CELL	1,28	0,07	0,47
SILICONE FOAM	1,10	0,44	0
OIL	1,13	0,49	0,01
LACING TAPE GE POLYESTER	1	0,07	
GRAPHITE/EPOXY	0,57	0,01	0,09
EPOXY FIBERGLASS BOOM CYLINDER	0,20	0,05	0,08
KEVLAR/PHENOLIC HONEYCOMB CORE	2,70	0,01	2,28
LAMINATE KEVLAR EPOXY/SILICONE/MASK COMPOSITE	1,14	0,11	0,21
LAMINATE KEVLAR/EPOXY	1,79	0,02	0,78
LAMINATE SHIM ALUMINUM	0,05	0	0,1
PYRALIN 12 POLYMIDE PREPREG	0,52	0	

Table 2.2: TMT, CVCM and WVR values for materials

2.3 Effect of radiation on materials

Spacecraft during their operational life are subjected to radiation bombardment as a result of certain phenomenologies from sources outside the spacecraft or inside. These effects cause a degradation of the characteristics of aerospace materials leading to a reduction in safety conditions. The external phenomenology has been extensively discussed in the previous chapter, so only the main complications deriving from the continuous exposure and possible methodologies to reduce these phenomena will be introduced. In general the properties that are most affected can be summarized in [18]:

- **Mechanical properties**: reduction of tensile strength, flexibility, fatigue and hardness of the material;
- **Thermal properties**: there is a significant change in the thermal conductivity of materials;
- **Optical properties**: changes may concern the degree of emissivity or absorption of the material;

The radiation sources inside the spacecraft are derived from nuclear reactors for propulsion and electricity as well as from energy sources powered by radioisotopes. To determine the importance of defects affecting the material, several factors such as pressure and temperature conditions, or material sensitivity, as well as mission profile must be considered. In order to be able to analyze and assess whether a certain material can be used for a given mission, several steps are followed. In particular, it assesses the external and internal environment to which spacecraft will be subject (as a result it analyzes the energy reduction of each radiation as well as the exposure time) and the internal environment. Subsequently, the materials are checked to determine the effect produced by the operating conditions with particular regard to the critical condition of the material (the data are then tabulated). Finally, after selection of the material of each application, analysis of the finished design is carried out to determine that all systems operate in the correct way and according to the required specifications.
Radiation analysis is quite complex as it must be considered that some radiations have fluctuating energy streams and spectra that lead to uncertainty of the results.The main iterations concerning radiation and matter can be divided into two main groups:

- collisions, in ordered solids, of atomic displacements;
- collisions involving ionisation and the production of free radicals (radiochemical phenomena);

Tests have been carried out over the years to assess the influence of radiation, but the latter rarely represented the actual operating conditions [18]. In general, it has been concluded that the mechanical properties of metals and ceramics do not vary significantly if they are subject to the following conditions:

- Proton flux with an energy exceeding 1MeV;
- Neutron flux having an energy exceeding 1 Kev;
- electron flux with an energy exceeding 1 Mev;

While polymeric materials exhibit radiation variations with significant changes in material characteristics [18].
Entering more in detail it can be observed that the particles and the photons can cause the marriages of the atoms through the iteration with the solids, and these derive from the rupture of the chemical bonds that are provoked from the dispersion of an energetic particle (by an atomic nucleus) [18]. As a result, the atom, moving, is able to create secondary displacements and, sometimes, also to ionize other atoms during its journey. Analyzing in detail the effects produced by each single element it can be noted that neutrons, protons and alpha particles produce changes on solids in a macroscopic way unlike the displacements produced by electrons. In general, electronic excitation is directly created when a material is irradiated by electrons, gamma, ions or protons, but in some cases this may result from a high neutron irradiation rate which, as a result of excessive acceleration, exceeds the velocity of an electron in the outermost shell of the atom which will therefore tend to lose electrons.
In addition, in order to assess the intensity of radiation is used as a reference rad (absorption of 100 ergs per gram of material) associated with a specific material, while the linear energy transfer rate (mainly describes the intensity of localized ionization) is expressed in KeV.

2.3.1 Effects of radiation on metals

On metals the main effect that is produced is the creation of interstitial atoms and reticular spaces within the structure of the metal and this causes a decrease in the density of the material due to the overall expansion produced by the radiation (Fig. 2.6). Consequently, studies conducted [18] have shown that inside the metal there is a decay of tensile strength, creep, fatigue, ductility and plasticity in favor of an increase of overall hardness of the material.The plasticity is modified due to radiation exposure as the phenomenon is closely linked to the movement of dislocations that are blocked by the formation of interstitial groups.

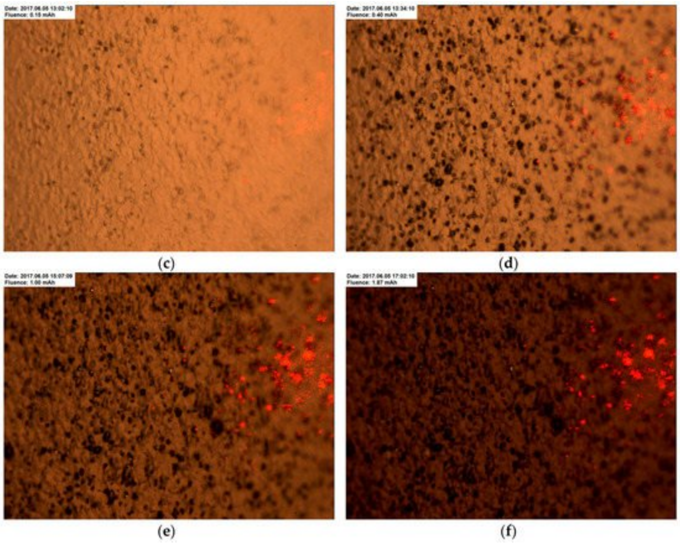

Figure 2.6: Effect of radiation on metals

In addition, the consequences of neutron irradiation strongly depend on the time and temperature of exposure as well as the energy spectrum.
As previously mentioned, the mechanical characteristics of metals tend to vary as a result of this phenomenon and in particular, various studies [18] have shown that significant variations occur on the transition from brittle-ductile fracture (occurs at higher temperatures), on the creep-rate and stress-ruptures properties (in this case the variation mainly affects the direction and the amplitude of the variations) and finally a decrease in density.
Finally, it is possible to mention the effect of radiation on metal-to-metal welded joints, and in particular studies have shown [18] that there is an increase in tensile strength when stainless steel type 30 I is used, while it is possible to observe a decrease in tensile strength for aluminium type 2014 T6. In conclusion it can be noted that the values and data used so far have a wide range of uncertainties as the changes depend on numerous factors.

2.3.2 Effect of radiation on polymers

In general, polymers are highly influenced by radiation and it is complex to analyse the variations in mechanical, physical and chemical characteristics as not all are similarly affected by radiation. In addition, radiation-induced excitation is often localized with a specific bond and this can cause considerable instability that is usually filled with the addition of aromatic rings that redistribute excitation energy throughout the material [18].

Polymers that are exposed to radiation are characterized by different types of behavior (Fig. 2.7):

- **cross linking**: as a result of this type of reaction, molecular weight increases as chemical bonds are created between two adjacent polymeric molecules. Finally, the material is bound in an insoluble three-dimensional net;

- **chain scission**: this type of reaction leads, on the other hand, to an increase in solubility and a decrease in molecular weight;

The latter can cause effects inside the polymer such as a reduction of the Young module of the material, an increase in elongation or a decrease in the hardness of the material itself and, finally, may cause hydrogen to enter and release, which may cause an increase, in some cases, of thermal conductivity.
Another effect to consider is the presence of oxygen that can change the degree of modification of a polymer even if the oxygen-related mechanism has not yet been found. In general, research has shown that it takes over reactions after the production of free radicals.
As for adhesives, the latter, being organic based, are very sensitive to the effect of

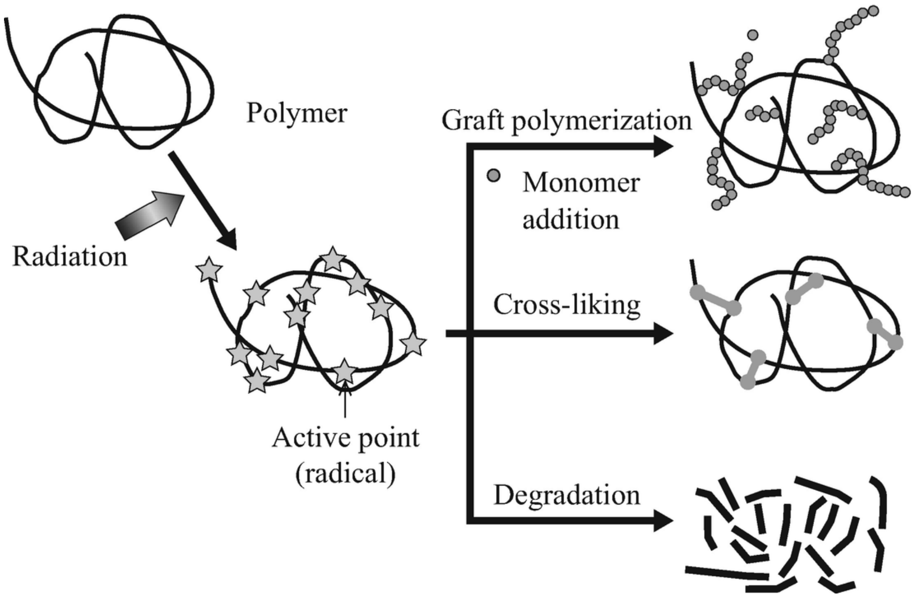

Figure 2.7: Reactions of polymers to the effect of radiation

radiation that is usually evaluated by measuring the variations in shear strength, tensile strength and fatigue. It has also been noted that, usually, the adhesives used for applications with high temperature [18] are those that most resist to radiation (epoxy, vinylphenol). Finally, in order to improve overall stability, fillers are added

to adhesives even if this sometimes leads to a reduction in shear strength.
Elastomers, on the other hand, among polymeric materials, are those that are most influenced by radiation. In particular, it has been demonstrated [18] that temperature has a predominant effect on radiation damage as well as the presence of oxygen. The application of static or dynamic loads can also be a factor that varies the effect of radiation. Moreover, elastomers, when exposed to UV rays, tend to evaporate volatile by-products with a low molecular weight causing a change in material properties (the same degree of degradation is also visible when exposed to gamma rays).

2.3.3 Effect of radiation on Graphite and Ceramics

For ceramic materials there is no variation in characteristics as a result of radiation exposure when this is less than 109 rad [18]. When high values are reached, however, the effects begin to become more important (especially in ceramics containing beryllium and boron).
Graphite is very often used as a moderator in nuclear reactor systems, which is why a great deal of research has been done to assess its characteristics. From these it was found that the effects become important when the levels of influence of the electrons are very high and in general an increase of the hardness of the chemical reactivity and a reduction of the thermal conductivity has been observed.

2.4 Temperature

The thermal effects on the material involve a modification of the internal structure of the material and consequently on the properties of the material itself. Among the various consequences on the materials it is possible to underline the phase change, the dimensional change (consequent to the thermal expansion of the material), modifications linked to elasto-plastic characteristics of the material or even physical changes of the material itself (drying, change in colour).
It is also possible to point out that all materials, regardless of their characteristics, undergo decomposition at high temperatures, while for low temperatures there is mainly an increase in fragility.
As mentioned above, thermal loads produce internal variations in the material that involve a change in characteristics.
It must be considered, in fact, that energy modifies the equilibrium equations by adding an additional load. Moreover, studying the variation of the mechanical characteristics of the main materials, it has been noted that on average all these properties decrease with the increase of the temperature.

It has also been observed that small variations in size cause elastic deformation, but this disappears when the initial condition is recovered. If the material is also forced to move, the internal elastic stresses develop to accommodate the variation according to precise rules [19]. When temperature variations are high, however, non-elastic deformations occur within the material. The high temperatures produce a fusion in the material allowing the matter to move and reorder and, after solidification, new solid bonds are created.
The materials that are able to undergo these large deformations have high ductility and resistance, otherwise these internal phenomena can cause the infragilation and subsequent break of the material.
Another phenomenon strongly influenced by temperature is creeping (the latter has the characteristic of growing with time under constant load conditions). Creeping is also considered as the combined effect of deformation and temperature, in fact it is observed that the phenomenon occurs when the temperature is above $0.3T_m$ [19] (melting point of the material).According to Arrhenius law, moreover, creeping, and the time until the break, vary according to an exponential law.

$$t_{break} = a\sigma b e^{\left(\frac{T_a}{T}\right)} \tag{2.10}$$

Where σ is the voltage applied while a, b t T_a are empirical values attributable to a particular material.
An important effect (especially within the space environment) is the temperature gradient and one of the main parameters related to the material that are affected by this phenomenon is thermal conductivity. In general it is possible to connect the temperature gradient with the thermal conductivity of the material. In fact, considering a bar with cross-section A it is possible to relate the heat that flows along a certain direction with the difference in temperature in two different parts by means of the following formula [20]:

$$\frac{dQ}{dt} = -KA\frac{dT}{dx} \tag{2.11}$$

With K thermal conductivity of the material.
In this case it can be noted that the heat flow is opposite to the temperature gradient in the case of isotropic medium. If the latter condition is not present, heat flows may form which are not perfectly parallel to the temperature gradient.
The heat is carried along the solid through the vibration of the atoms that, through their oscillatory motion, move nearby atoms by moving heat. As a result, some materials have higher capacity to conduct heat.

2.4.1 Thermal protection system

Spacecraft during their operational life must perform numerous atmospheric and hypersonic flight maneuvers where the use of thermal protection systems is required

(Fig. 2.8 shows a thermal shield used for rientry maneuvers) [21].The selection of these materials depends on several factors including the environment and trajectory, so as to improve performance and a reduction in weight.Among the various techniques and materials used it was decided below to give higher priority to ultra-high temperature materials (UHTM) used for thermal protection systems (TPS). Studies

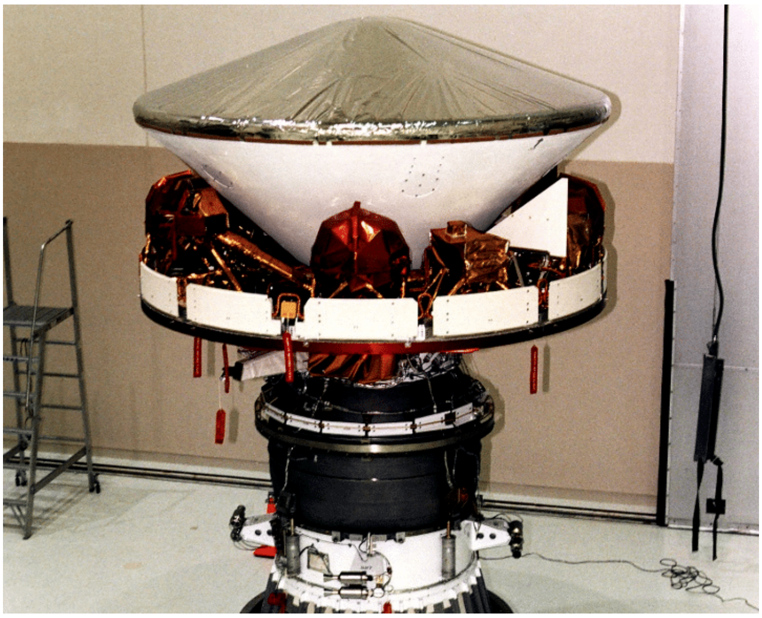

Figure 2.8: Thermal shield used for re-entry manoeuvres

and research conducted in recent years [21] have shown that, in order to protect materials from high temperatures, a thermal protection system is used designed in such a way as to possess a smooth and aerodynamic surface. As a result, future studies focused mainly on materials that could withstand high melting points as well as good performance during operational conditions.
All this has reduced the selection of materials to the only UHTM that provide high protection.
Typically, TPS were tiles, thermal blankets, and insulators that covered critical areas of an aircraft and almost completely protected the surface of the orbiter.
The following are the main elements used:

- **Silicon carbide (Sic)**It was used basically because it was very adaptable and also had a good strength and density not very high (similar to aluminum). It is used within the aerospace industry mainly as a reinforcing matrix (CMC), as a particulate filter in a ceramic composite (UHTC) or sometimes can be combined with carbon fibers in order to obtain materials that withstand even higher temperatures (Cmcs are created with non-oxide matric materials). A number of studies [21] have also shown that the degradation of carbon fibres occurs only at temperatures above 2600C in the non-oxidant atmosphere, and this has shown that the combination of Sic with carbon fiber leads to the protection of the latter that can then withstand higher temperatures. In fact, Sic, activating when the temperature exceeds 500°, creates a silica glass layer that protects carbon from oxidation;

- **Boron carbide**: It is mainly used as wear parts as it has a high strength and hardness. Various studies [21] have shown that the material has a higher temperature thermoelectric material (as a result it can be used as a first wall for a fusion reactor), moreover, it is a very reliable material from the performance point of view when there are particular applications for which it is important to have high mechanical characteristics;

- **Silicon boride**: in general these materials have high chemical resistance properties, and are used in many areas of materials for thermoelectric applications as they have good chemical stability, a high Seebeck coefficient, a high melting point and a high thermal conductivity.

- **Zirconium and hafnium diborides**: UHTCs with these elements are among the most used and famous in the world because of their high resistance to oxidation and temperatures. Studies [21] have shown the considerable importance these have above all for the high thermal conductivity they possess;

Chapter 3

Madflex

The Madflex is a new and innovative material designed by Composite Reasearch (Core) and is a material structured as a sandwich. The particularity of the material lies in its characteristics, in fact if one of the two faces is loaded the latter is non-deformable, while if it is loaded on the other face the material deforms (Fig. 3.5).
In addition to the latter feature, the Madflex has several advantages, which can be listed below:

- Resistance to chemical agents;
- Resistance to temperature;
- Anti-seismic;
- flame retardant;
- Endless surface finishing;

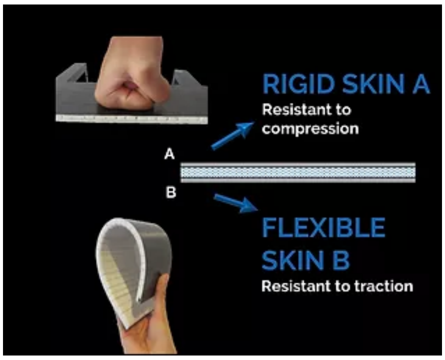

Figure 3.1: Double behavior of Madflex

The Madflex, in addition to the characteristics described above, is a very light material (Fig. 3.2), in fact comparing it with an ABS sheet (considering the configuration in which one of the two faces is made of aluminum) has a weight that is about 5 -6 times less with the same flexural resistance.In addition, its insulation capacity (Fig 3.4) exceeds five times that of a sheet of ABS.
The Madflex is a material that releases a very low level of CO2 (Fig. 3.3)during the production process, therefore, comparing it with the same ABS panel, releases half of the greenhouse gases into the environment and can therefore be considered as an ecological material.
Finally, it is easily deformable through the use of moulds (thermoformable) and is easily transportable as it can be rolled on one side.
The material of the face can also be different and can range from carbon fibers, glass fibers up to even Kevlar fibers. As a result, the data for a part of these configurations will be entered below. In the Table 3.1 were inserted the main values related to the mechanical properties of Madflex derived from experimental tests.

	Test Method	Max value configurations	Min Value configurations
Bending Stiffness (rigid side) $[\frac{Nm^2}{m}]$	ASTM D7250/D7520M	250	13
Bending Stiffness (rollable side)$[\frac{Nm^2}{m}]$	ASTM D7250/D7520M	2,0	0,1
Tensile strength$[\frac{KN}{m}]$	ASTM D3039/D3039M	700	350
Flexural strength MPa	ASTM D7250/D7250M	450	95
Flatwise compressive strength MPa	ASTM C365/C365M	2,4	1,2

Table 3.1: Madflex Mechanical Properties

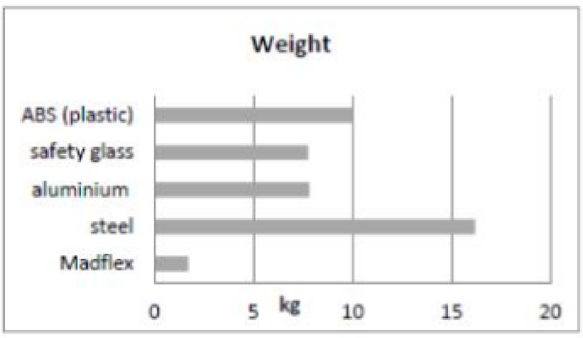

Figure 3.2: Comparison in terms of weights of 1 $m2$ sheets in different materials

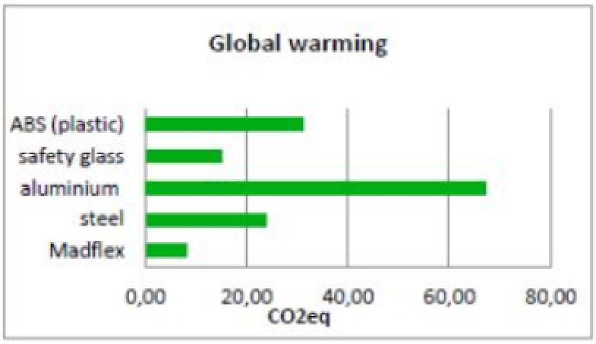

Figure 3.3: Comparison in terms of CO2 of 1 $m2$ sheets in different materials

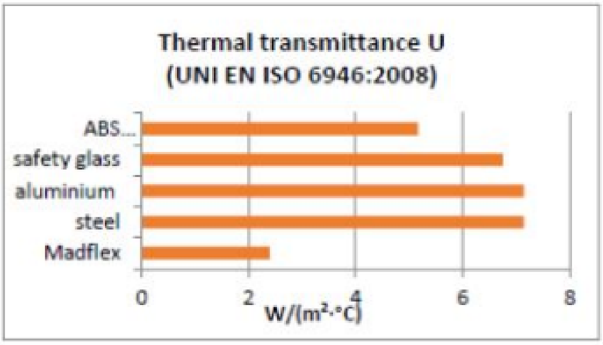

Figure 3.4: Comparison in terms of Thermal trasmittance you 1 $m2$ sheets in different materials

	Thickness	Areal weight	Tensile strength	Failure bending moment	Bending stiffness (rigid)	Bending stiffness (rollable)	Flatwise compressive strength
Unit	mm	$\frac{kg}{m^2}$	$\frac{kg}{m}$	$\frac{Nm}{m}$	$\frac{Nm^2}{m}$	$\frac{Nm^2}{m}$	MPa
Value	5	1,3	500	170	30	0,5	1,7
test			ASTM D3039/ D3039M	ASTM D7250/ D7250M	ASTM D7250/ D7250M	ASTM D7250/ D7250/M	ASTM C365/ C365M

Table 3.2: Properties of first type of Madflex (Madflex 1.0) produced by Composite Reasearch

	Thickness	Areal weight	Tensile strength	Failure bending moment	Bending stiffness (rigid)	Bending stiffness (rollable)	Flatwise compressive strength
Unit	mm	$\frac{kg}{m^2}$	$\frac{kg}{m}$	$\frac{Nm}{m}$	$\frac{Nm^2}{m}$	$\frac{Nm^2}{m}$	MPa
Value	11	1,8	700	480	240	1,5	1,5
test			ASTM D3039/ D3039M	ASTM D7250/ D7250M	ASTM D7250/ D7250M	ASTM D7250/ D7250/M	ASTM C365/ C365M

Table 3.3: Maximum capacity and structural performance and it can be used to replace structural metallic part

	Thickness	Areal weight	Tensile strength	Failure bending moment	Bending stiffness (rigid)	Bending stiffness (rollable)	Flatwise compressive strength
Unit	mm	$\frac{kg}{m^2}$	$\frac{kg}{m}$	$\frac{Nm}{m}$	$\frac{Nm^2}{m}$	$\frac{Nm^2}{m}$	MPa
Value	6	1,65	450	230	40	0,6	1,8
test			ASTM D3039/ D3039M	ASTM D7250/ D7250M	ASTM D7250/ D7250M	ASTM D7250/ D7250/M	ASTM C365/ C365M

Table 3.4: First version of Madflex shear resistant, and high resistance to perforation

	Thickness	Areal weight	Tensile strength	Failure bending moment	Bending stiffness (rigid)	Bending stiffness (rollable)	Flatwise compressive strength
Unit	mm	$\frac{kg}{m^2}$	$\frac{kg}{m}$	$\frac{Nm}{m}$	$\frac{Nm^2}{m}$	$\frac{Nm^2}{m}$	MPa
Value	5,5	175	500	225	55	0,4	1,7
test			ASTM D3039/ D3039M	ASTM D7250/ D7250M	ASTM D7250/ D7250M	ASTM D7250/ D7250/M	ASTM C365/ C365M

Table 3.5: Another version of Madflex shear resistant

The Madflex has the characteristic of being asymmetrical, and this is mainly due to the fact that the upper and lower skins have different materials as well as a different thickness (Fig. 3.5). This different property results in a different behavior of the Madflex when it is stressed to traction and compression on one side and on

the other. In fact, one of the two skins is usually composed of a material that has a high elastic modulus both tensile and compression (carbon fibers usually but also glass fibers)while the other face is formed by a skin composed of a low compression module (for example, Dyneema may be used).
Consequently, when the Madflex is loaded along the rigid side the rigid skin assumes a rigid compression behavior while it is flexible in traction and can withstand in this case the application of high loads (Fig. 3.6).
Conversely, if the flexible side is loaded, having a very low compression module, it cannot resist high compressions. In summary the sandwich is able to resist on

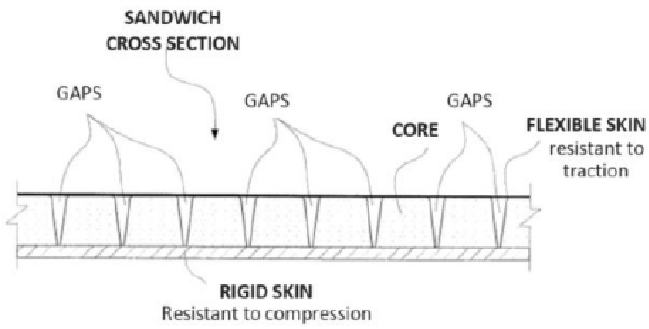

Figure 3.5: Interior of the madflex

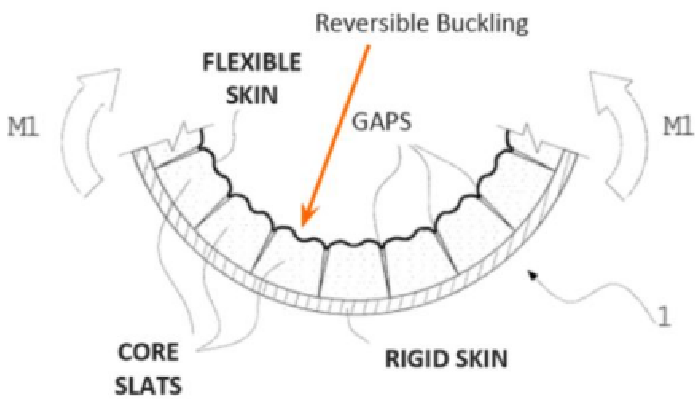

Figure 3.6: Madflex behavior in a bending configuration

one side while remaining rigid, while on the other it can bend.
The behavior of the material can be schematized as in Fig.3.7 or as a non symmetrical sandwich that has two different Young modules and different thicknesses on

both sides.
In order to be able to derive the bending stiffness must take into account this behavior and must be first found the position of the neutral axis. The latter is given by those coordinate values at which the moment of area is zero as a result of integration along the cross-section.
The bending stiffness may be calculated as follows [22]:

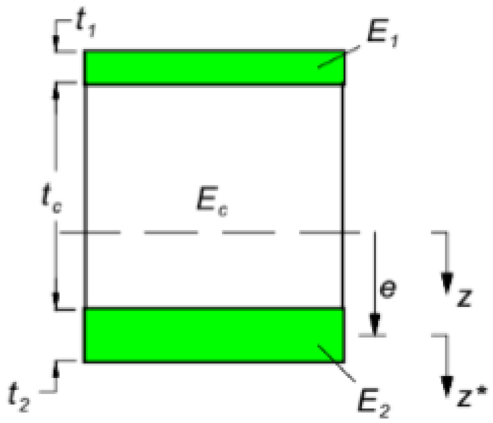

Figure 3.7: non-symmetrical sandwich

$$D = \int E z^2 dz \tag{3.1}$$

Which, in the case of symmetrical sandwiches leads to:

$$D = \frac{E_f t_c^3}{6} + \frac{E_f t_f d^2}{2} + \frac{E_c t_c^3}{12} \tag{3.2}$$

While in the present case it is modified to take into account the different characteristics of the faces.

$$D = \frac{E_1 t_1^3}{12} + \frac{E_2 t_2^3}{12} + \frac{E_c t_c^3}{12} + E_1 t_1 (d-e)^2 + E_2 t_2 e^2 + E_c t_c \left(\frac{t_c + t_2}{2} - e\right)^2 \tag{3.3}$$

where e is equal to the distance between the neutral axis of the lower face and the mean axis and can be calculated as:

$$E_1 t_1 \left(\frac{t_1}{2} + t_c + \frac{t_2}{2}\right) + E_c t_c \left(\frac{t_c}{2} + \frac{t_2}{2}\right) = e \left[E_1 t_1 + E_c t_c + E_2 t_2\right] \tag{3.4}$$

while d is the distance between the center of the two faces.
Equation 3.3 can be simplified by introducing two different simplifications: in the

first case it is possible to assume that $E_c << E_f$, while in the second case that $E_c << E_f$ and thin faces. This leads to the following formulations.

$$\bar{D} = \frac{E_1 t_1^3}{12} + \frac{E_2 t_2^3}{12} + \frac{E_1 t_1 E_2 t_2 d^2}{E_1 t_1 + E_2 t_2} \tag{3.5}$$

and,

$$\bar{D} = \frac{E_1 t_1 E_2 t_2 d^2}{E_1 t_1 + E_2 t_2} \tag{3.6}$$

It is also useful to assess the state of stress and deformation of the structure and this can be done if the Euler-Bernoulli beam theory is introduced for an isotropic and homogeneous material. From this theory it is possible to deduce that each material, subjected to a bending moment, tends to develop a curvature according to the following formulation:

$$M = \frac{EI}{r} = \frac{bD}{r} \tag{3.7}$$

where EI indicates bending stiffness while r is the radius of curvature and b represents the width of the test piece.

From the formula it is possible to deduce that, at the same bending moment, higher bending rigidities result in lower curvatures radii. The faces are thin, therefore introducing this simplification within equation 3.3 simplifies different relationships, arriving at the following final formulation:

$$EI = \left(E_f \frac{bt^3}{6} + E_f \frac{btd^2}{2} + E_c \frac{bc^3}{12} \right) \tag{3.8}$$

It is also important to note that equation 3.8 is valid only in the case of a symmetric sandwich (situation not consistent with Madflex).

At this, the transverse displacement of the W_1 beam can be estimated using the same theory. In fact it can be considered a case of simple bending in which a beam is stressed by a central load, by theory the stressed cross-sections remain perpendicular to the longitudinal axis (as per hypothesis). In this case the lower face is placed in tension, while the upper one is placed in compression.

Along the core, however, there is at each section shear stress that brings a shear deformation equal to $\frac{Q}{Gbd}$ with G material shear module, while b and d are geometric characteristics of the beam. The effect of the cut changes the shift before an amount equal to W_2 associated with the deformation of the sandwich core:

$$\frac{dw_2}{dx} = \gamma \frac{c}{d} = \frac{Q}{Gbd} \frac{c}{d} = \frac{Q}{AG} \tag{3.9}$$

The final displacement at the midpoint is equal to the sum of the two abovementioned effects:

$$\Delta = \frac{WL^3}{48D} + \frac{WL}{4AG} \tag{3.10}$$

The behavior of Madflex is also closely linked to a phenomenon of local instability affecting the material and leading to double behavior. This phenomenon affects the flexible skin of the material and is called "local buckling". As a result the skin can fail if two different conditions occur: Dimpling (a sandwich can fail if one of the two faces is not supported by an underlying layer of foam), Wrinkling ("Face wrinkling is a buckling mode of the skin with a wavelength greater than the cell width of the honeycomb core under compression load").
Finally, it is important to underline the importance that foam and gluing have on the Madflex. In fact, the rigid skin, despite having a higher resistance, is still subject, because of its reduced thickness, to a local instability that may occur before the ultimate compressive strength is reached. In order to reduce this phenomenon it is therefore important to pay particular attention to the type of schuma and the bonding that is carried out.

3.1 Madflex for Space Applications

The Madflex allows, as mentioned above, to have a double behavior if stressed as a result, thanks to the thermal characteristics and low weight, assumes considerable interest in the applicability to space aircraft.
Possible uses include:

- reliable and lightweight hinges;
- habitats usable for human missions to the Moon and Mars;
- for the support of solar panels (ROSA);
- skin for expandable space modules;

The following is a possible configuration (Fig.3.8, 3.9, 3.10).

Figure 3.8: New configuration for space use

Figure 3.9: Double test behaviour subjected to bending

Figure 3.10: Double test behaviour subjected to bending

The core was made of Rohacell hero foam 110 innovative, light, economical.

This type of foam offers high mechanical properties against a reduced weight as it is characterized by a closed cell structure. In addition, the Rohacell is heat resistant up to temperatures of about 210 C and allows it to be processed with techniques such as RTM and VARTM.
The first layer is composed of pre-impregnated carbon with high modulus fibers of Young and epoxy resin resistant to medium temperatures and with a high impact resistance (in table 3.7 the main features are shown). While the second skin consists of two layers of polyurethane between which is inserted a layer of kevlar (in table 3.8 the main features are shown). Inside the core, there are also empty spaces, as seen in the figures 4.17 and 3.5.
In the table 3.6 the main characteristics are inserted:

Property	Rohacell 110 Hero
Density	110 $\frac{Kg}{m^3}$
Compressive modulus	83 MPa
Tensile Strength	6,3 MPa
Tensile Modulus	189 MPa
Elongation at break	9,9 %
Shear Strength	2,3 MPa
Shear Modulus	50 MPa
Maximum Shear Strain	7,2 %
Coefficient of thermal Expansion	3,77 $\frac{1}{K}10 - 05$

Table 3.6: Properties of Rohacell 110 Hero

Property	Prepreg Carbon
Density	1,5 $\frac{Kg}{mm^3}$
Thickness	0,23 mm
Young Modulus (along fiber direction)	120 GPa
Young Modulus (trasversal direction)	4 GPa
Poisson's Ratio	0,3
Shear Modulus	5 GPa

Table 3.7: Main features pre-impregnated carbon

Property	Kevlar
Density	1,44 $\frac{Kg}{mm^3}$
Thickness	0,23 mm
Young Modulus (along fiber direction)	6 GPa
Young Modulus (trasversal direction)	1 GPa
Poisson's Ratio	0,3
Shear Modulus	1 GPa

Table 3.8: Main features Kevlar

Chapter 4

Test for Flexural Properties

In the following chapter a main phase is inserted for the characterization of a new material, that is the step of test. The main objective is to understand the behavior of the material when subject to certain stresses and under certain conditions of constraint and to have a more precise estimate of the mechanical properties of the material. The methods that can be used to make an estimate are primarily analytical, experimental or FEM analysis.
The sample of the material which will be subject to testing, has a length of about 200mm and a width of 19 mm.
In the table 4.1 are inserted the main data of the experimental analysis.

Sample length	200 [mm]
sample width	19 [mm]
Core thickness	5 [mm]
Upper face thickness	0,23 [mm]
Lower face thickness	0,23 [mm]
Distance of load application points	35 [mm]
Distance between the two supports	80 [mm]

Table 4.1: Data for the experimental test

4.1 Analytical Formulation

The analytical formulation allows to evaluate the flexuous stiffness of the sandwich through the law proposed by Allen. According to the proposed theory it is possible to calculate the EI using the stiffness of the skins and the core measured with respect to the neutral axis and the characteristic dimensions of the sandwich

The flexural stiffness of the core can be assessed by the following formulation:

$$EI_{core} = \frac{b_c c^3}{12} E_c \tag{4.1}$$

For the inertia of the two faces the following law can be used instead:

$$I_{face} = 2\left[I_{faces} + A\left(\frac{d}{2}\right)\right] \tag{4.2}$$

From which:

$$EI_{faces} = E_f\left[\frac{b_c t^3}{12} + \frac{b_c t d^2}{2}\right] \tag{4.3}$$

with:

- b_c equal to the core length;
- c equal to the core height;
- t equal to the faces thickness;
- d equal to the distance from the average axis;

Finally, through the use of ASTM it is possible to calculate the bending stiffness and deflection of the beam, and in Figure 4.1 a beam with the useful distances is schematized:

$$EI = E_f\left[\frac{b_c t^3}{6} + \frac{b_c t d^2}{2}\right] + \frac{b_c c^3}{12} E_c \tag{4.4}$$

$$\delta = \frac{F(2b^3 - 3ba^2 + a^3)}{96EI} + \frac{F(b-a)}{4U} \tag{4.5}$$

The above formulation is valid in the case of symmetric Sandwich, but since the test material is not symmetrical, it was considered appropriate to use equation 3.5 in both the rigid and the flexible case.
In the rigid case, that is when the sandwich is in traction, one has a contribution of the two faces (the contribution of the core has been neglected) one has that:

$$\bar{D} = \frac{E_1 t_1^3}{12} + \frac{E_2 t_2^3}{12} + \frac{E_1 t_1 E_2 t_2 d^2}{E_1 t_1 + E_2 t_2} \tag{4.6}$$

Multiplying the previous result by the width:

$$EI = bD = 0{,}6855[Nm^2] \tag{4.7}$$

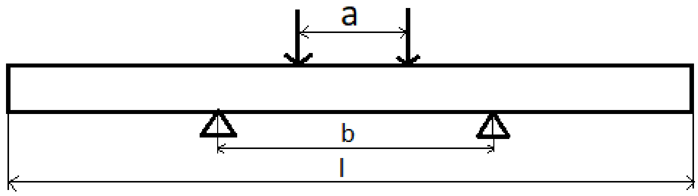

Figure 4.1: 4-point bending test measures

With b equal to the width of the test piece. In the flexible case (in compression) the only contribution is that relative to the upper face from which it is obtained (using the beam assumption) that :

$$EI = E_1 \frac{bt_1^3}{12} \tag{4.8}$$

$$EI = 0{,}0026[Nm^2] \tag{4.9}$$

Considering a thickness of the rigid layer equal to 0,24, and a Young module equal to 120 GPa, while for the flexible part a thickness of 0,23 mm and a Young module equal to 6 GPa

4.2 TEST Methods

The standard that is usually used to perform a bending test is ASTM D7250/7250M [23] on sandwich structures therefore in order to evaluate this characteristic also on the samples was made the same test (Fig.4.2). As per regulations, the test was done on 5 different tests on one side and on the other (as, as mentioned in chapter 3, the material has a double property), for a total of 10 samples. In addition, the geometry must respect certain constraints:

- the thickness of the specimen shall be the same as that of the component to be printed;
- The beam width shall not be less than twice the total thickness the beam (or three times the thickness of the heart);

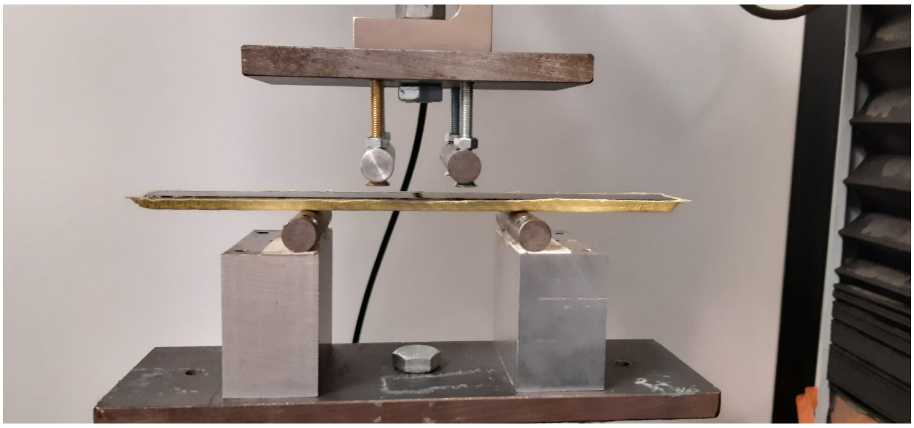

Figure 4.2: 4-point bending test machine

- The width of the beam must never exceed half the width of the supports on which the beam is stationed;

In the test carried out (Fig. 4.2) the bearings were inserted at a distance of about 60 mm from the ends, while the forces were applied at about 20 mm from the centre line. The test was carried out trying to get as close as possible to the conditions required by the legislation, and, once completed, the values for deformation and load were taken and the appropriate analyses were carried out. In particular, in order to obtain the bending stiffness of the beam it was considered appropriate to use the principle of virtual works. Once the unit load is applied, it is possible to evaluate the bending component due to the application of the force:

$$w = \int_{-b/2}^{b/2} \frac{M^a M^b}{EI} \, dz \tag{4.10}$$

Which applied to the present case:

$$w = \frac{F}{2EI} \left[\frac{b^3}{24} + \frac{a^3}{48} - \frac{a^2 b}{16} \right] + \frac{F}{4GA*} (b - a) \tag{4.11}$$

$$\epsilon = \frac{h}{2EI} \frac{F}{2} \left(\frac{b}{2} - \frac{a}{2} \right) \tag{4.12}$$

With equal to the distance of the application of the forces from the centre line, while b equal to the distance from the centre line of the supports.

4.3 Results flexible part

The test described above was carried out on five different test pieces, first on the flexible part and then on the rigid one. Table 4.2 shows the deformation values of two of the five samples as well as the force and time. In Figures 4.3, 4.4, 4.5, 4.6, 4.7, load trends as a function of deformation were inserted in the five samples and a final comparison was made (Fig. 4.8). From the diagrams the linear part has been extracted in order to be able to identify the flexural stiffness of the specimens.

Time [s]	w [mm]	Force [kg]	Time [s]	w [mm]	Force [kg]
17.0000	0	0.7800	17.0000	0	0.7700
33.0000	0	0.7800	34.0000	0	0.7700
50.0000	0	0.7700	50.0000	0	0.7700
67.0000	0	0.7700	68.0000	0	0.7700
83.0000	0	0.7800	84.0000	0	0.7700
100.0000	0	0.7800	100.0000	0	0.7700
117.0000	0	0.7800	118.0000	0	0.7700
133.0000	0	0.7700	134.0000	0	0.7700
150.0000	0	0.7700	150.0000	0	0.7700
167.0000	0	0.7800	168.0000	-0.0033	0.7700
183.0000	0	0.7800	184.0000	-0.0033	0.7700
200.0000	-0.0033	0.7800	200.0000	-0.0033	0.7700
217.0000	-0.0033	0.7800	218.0000	-0.0033	0.7800
234.0000	-0.0033	0.7800	234.0000	-0.0067	0.7800
250.0000	-0.0033	0.7700	251.0000	-0.0067	0.7800
268.0000	-0.0067	0.7700	267.0000	-0.0067	0.7700
283.0000	-0.0067	0.7700	284.0000	-0.0100	0.7700
300.0000	-0.0067	0.7800	301.0000	-0.0100	0.7800
317.0000	-0.0100	0.7800	317.0000	-0.0133	0.7800
334.0000	-0.0100	0.7700	334.0000	-0.0133	0.7800
351.0000	-0.0133	0.7700	351.0000	-0.0133	0.7800
367.0000	-0.0133	0.7700	367.0000	-0.0167	0.7800
383.0000	-0.0167	0.7700	384.0000	-0.0167	0.7800
400.0000	-0.0167	0.7900	401.0000	-0.0200	0.7800
417.0000	-0.0200	0.7900	417.0000	-0.0200	0.7700
433.0000	-0.0200	0.7900	434.0000	-0.0233	0.7700
450.0000	-0.0233	0.7700	450.0000	-0.0267	0.7800
467.0000	-0.0267	0.7700	468.0000	-0.0267	0.7800
483.0000	-0.0267	0.7600	484.0000	-0.0300	0.7800
501.0000	-0.0300	0.7600	500.0000	-0.0333	0.7600
517.0000	-0.0300	0.7600	517.0000	-0.0333	0.7600
534.0000	-0.0333	0.7600	534.0000	-0.0366	0.7800
550.0000	-0.0366	0.7600	551.0000	-0.0400	0.7800
567.0000	-0.0366	0.7700	567.0000	-0.0400	0.7800
583.0000	-0.0400	0.7700	584.0000	-0.0433	0.7700

Table 4.2: Experimental results for 2 of the five samples (flexible part)

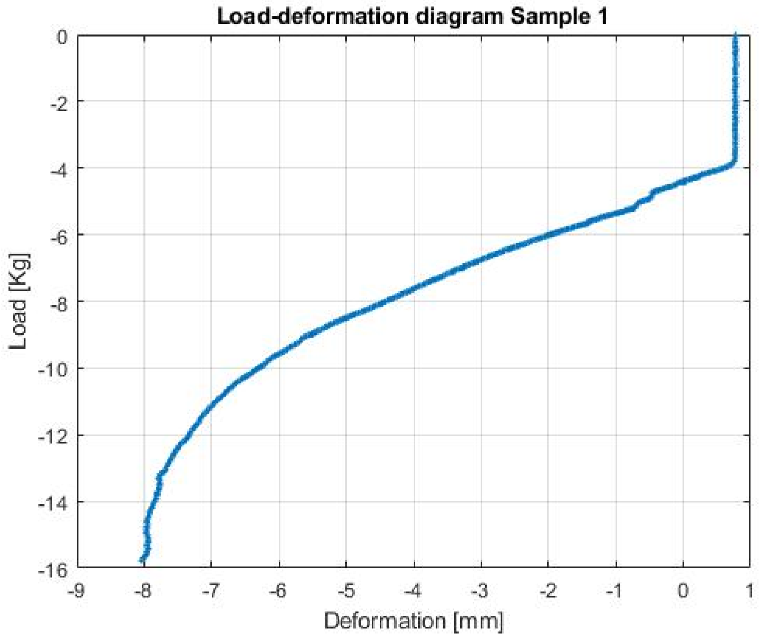

Figure 4.3: Load-deformation diagram for sample 1

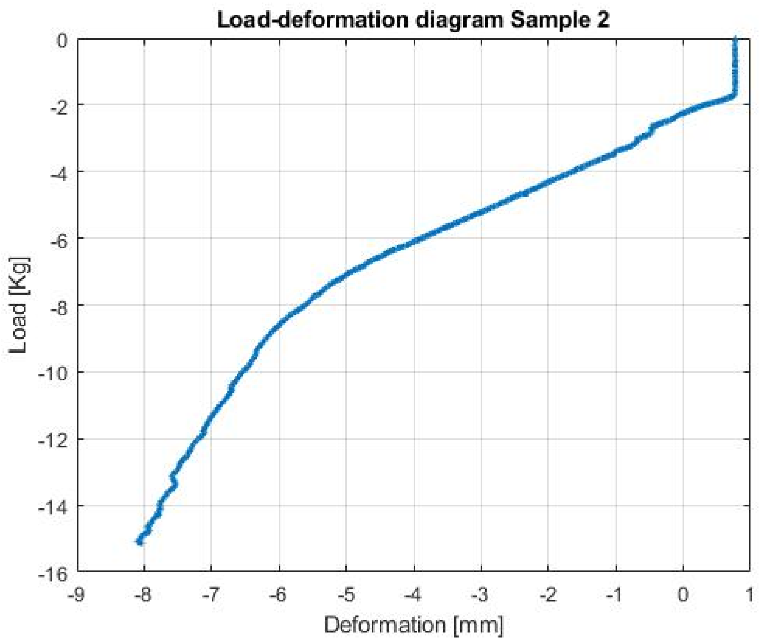

Figure 4.4: Load-deformation diagram for sample 2

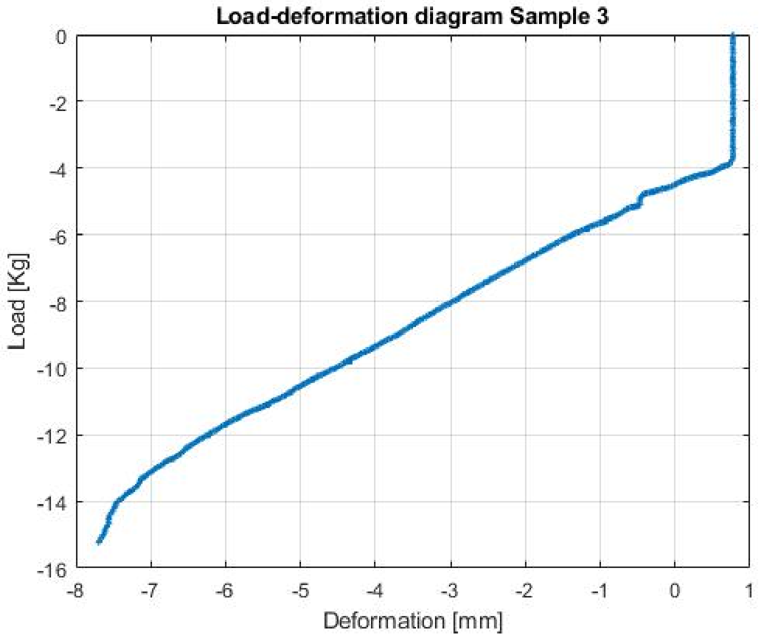

Figure 4.5: Load-deformation diagram for sample 3

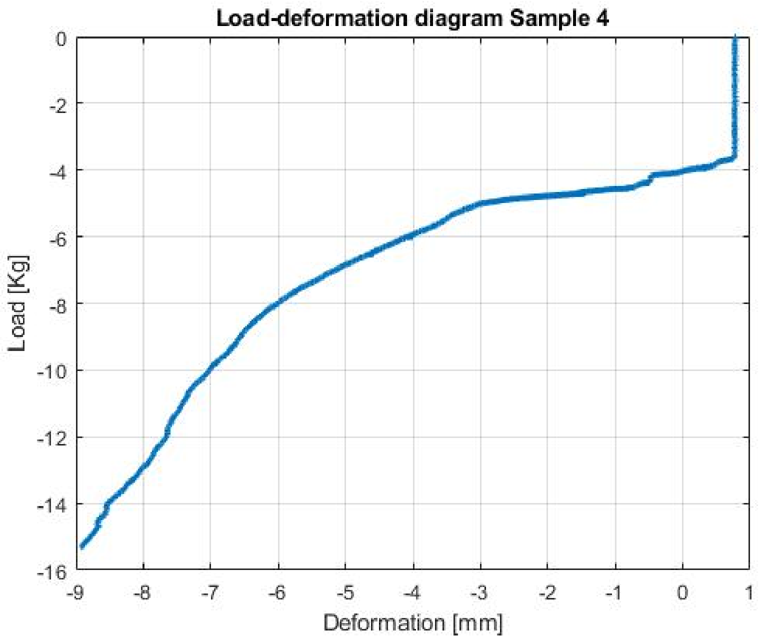

Figure 4.6: Load-deformation diagram for sample 4

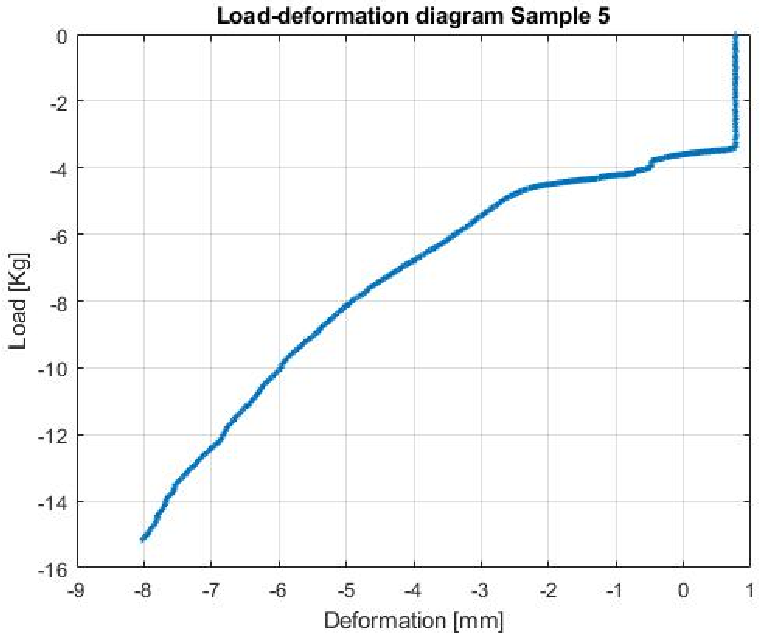

Figure 4.7: Load-deformation diagram for sample 5

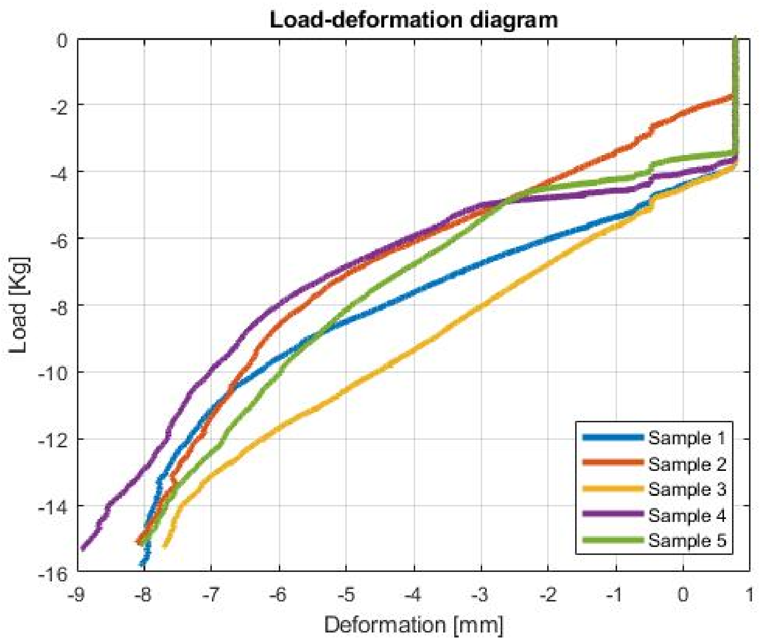

Figure 4.8: Load-deformation diagram for samples 1,2,3,4,5

Once the deformations related to the five specimens were identified, the equivalent stiffness of the flexible part was analysed. Below will be inserted, as an example, a graph (Fig.4.9) relative to the test five. In this case, as in the other test pieces, the test machine has been reset in order to avoid phenomena linked to the contact between the test machine and the test piece itself. In addition, it was considered appropriate to use equation 4.10 to calculate equivalent bending stiffness by disregarding the core effect. As can be seen from the figure above it has been

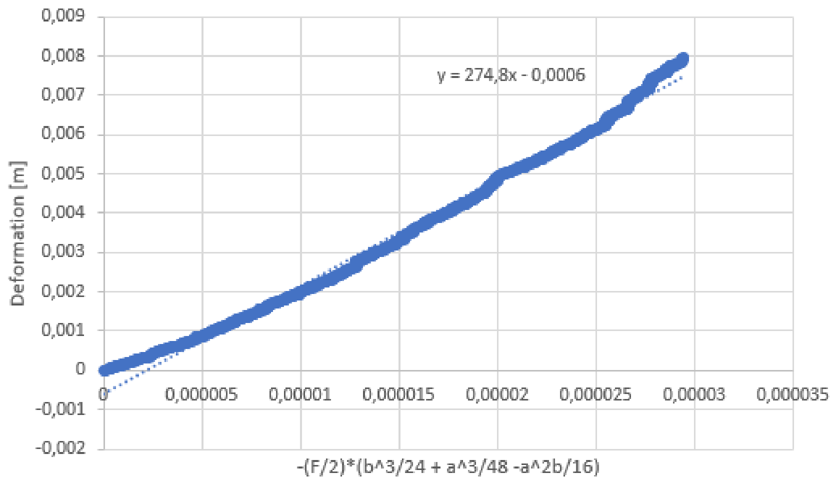

Figure 4.9: Analysis of the Equivalent stiffness of the fifth sample

possible to derive the stiffness through the inverse of the angular coefficient. For this reason, in the table 4.3 have been inserted the values related to the equivalent stiffness found in the five specimens.

Test sample	Equivalent Stiffness $[Nm^2]$
Nr.1	0,003192
Nr.2	0,00364
Nr.3	0,004475
Nr.4	0,003613
Nr.5	0,003639
Average value	0,003711
theoretical value	0,0026

Table 4.3: Equivalent Stiffness of the five samples (flexible part)

At this point it is possible to make comparisons between the various results obtained from the test, and in particular, with reference to the graphs showing the deformations of the specimens it is possible to note that there are no large deviations. In fact, after making an average between the various samples, it was possible to determine the relative error of the various curves with respect to the averaged value, from which it is clear that the deviations are of the order of 2-3%. Also in the table 4.4 relative errors in the calculation of the equivalent stiffness of the specimens are visible (average value equal to 0,003711 [Nm^2]).

Test Sample	error %|
Nr.1	16,25
Nr.2	1,95
Nr.3	17,07
Nr.4	2,71
Nr.5	1,97

Table 4.4: Relative error of test-piece Equivalent stiffness (flexible part)

In this case, it can be seen that all the test pieces have low relative errors, unlike the test piece 1 and 3 which have the greatest deviations.

4.4 Results Rigid part

As for the flexible part, in this case too, results for the first two tests have been included as an example (4.5). The results are shown in Figures 4.10, 4.11,4.12,4.13,4.14,4.15.

Time [s]	w [mm]	Force [Kg]	Time [s]	w [mm]	Force [Kg]
17.0000	0.5630	0.7700	17.0000	0	0.7800
33.0000	0.5630	0.7700	33.0000	0	0.7500
50.0000	0.5630	0.7700	50.0000	0	0.7500
66.0000	0.5630	0.7700	67.0000	0	0.7500
83.0000	0.5630	0.7700	83.0000	0	0.7800
100.0000	0.5630	0.7800	100.0000	0	0.7800
116.0000	0.5630	0.7800	117.0000	0	0.7800
133.0000	0.5630	0.7700	133.0000	0	0.7800
148.0000	0.5630	0.7700	150.0000	0	0.7800
166.0000	0.5630	0.7700	167.0000	0	0.7800
183.0000	0.5630	0.7700	183.0000	0	0.7800
215.0000	0.5630	0.7700	200.0000	0	0.7800
215.0000	0.5630	0.7700	216.0000	0	0.7800
237.0000	0.5597	0.7700	233.0000	0	0.7800
253.0000	0.5597	0.7600	250.0000	0	0.7700
269.0000	0.5597	0.7600	266.0000	0	0.7700
286.0000	0.5597	0.7600	284.0000	0	0.7700
303.0000	0.5597	0.7700	300.0000	-0.0033	0.7700
319.0000	0.5597	0.7700	317.0000	-0.0033	0.7800
337.0000	0.5597	0.7600	333.0000	-0.0033	0.7800
354.0000	0.5563	0.7600	350.0000	-0.0033	0.7800
370.0000	0.5563	0.7700	367.0000	-0.0033	0.7800
386.0000	0.5563	0.7700	383.0000	-0.0067	0.7800
402.0000	0.5530	0.7700	400.0000	-0.0067	0.7800
420.0000	0.5530	0.7800	417.0000	-0.0067	0.7800
436.0000	0.5530	0.7800	433.0000	-0.0067	0.7700
452.0000	0.5530	0.7700	450.0000	-0.0100	0.7700
468.0000	0.5497	0.7700	467.0000	-0.0100	0.7700
486.0000	0.5497	0.7700	483.0000	-0.0100	0.7700
503.0000	0.5497	0.7900	500.0000	-0.0100	0.7700
520.0000	0.5497	0.7900	517.0000	-0.0133	0.7800
536.0000	0.5463	0.7700	533.0000	-0.0133	0.7800
552.0000	0.5463	0.7700	550.0000	-0.0133	0.7800

Table 4.5: Experimental results for 2 of the five samples (rigid part)

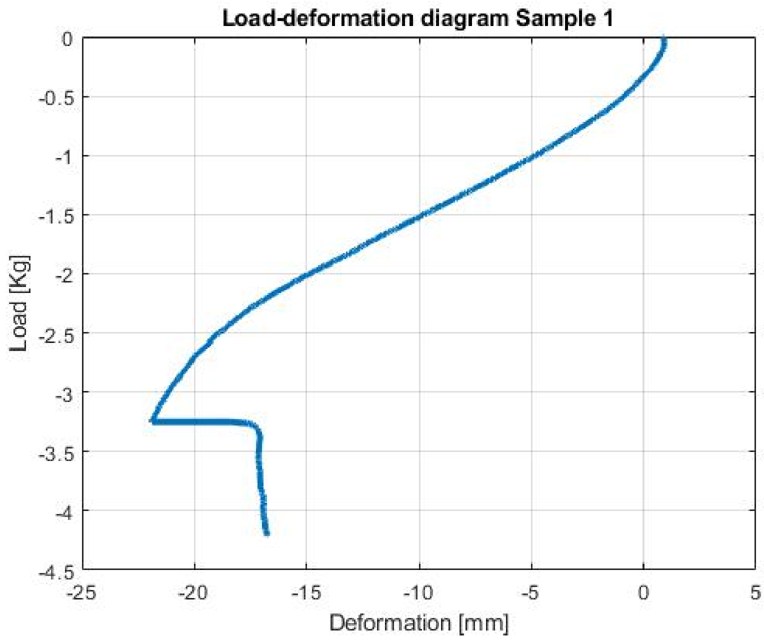

Figure 4.10: Load-deformation diagram for samples 1

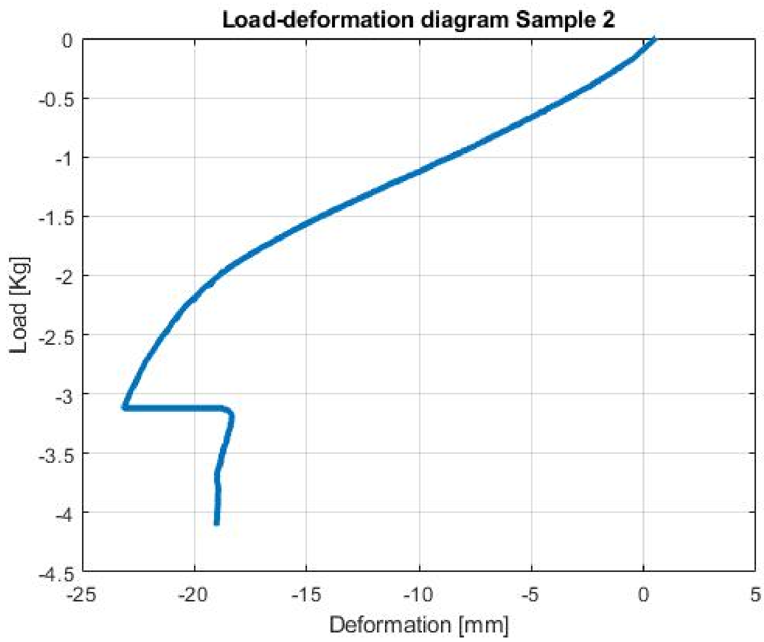

Figure 4.11: Load-deformation diagram for samples 2

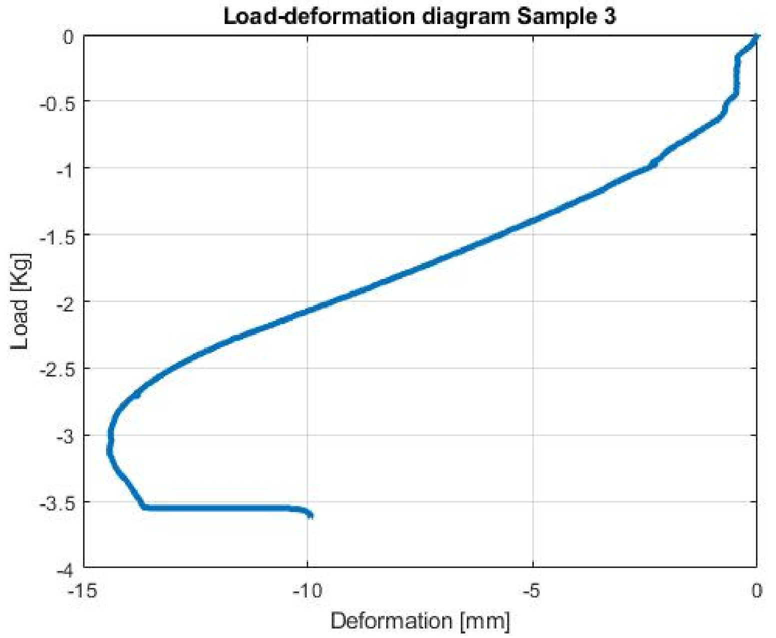

Figure 4.12: Load-deformation diagram for samples 3

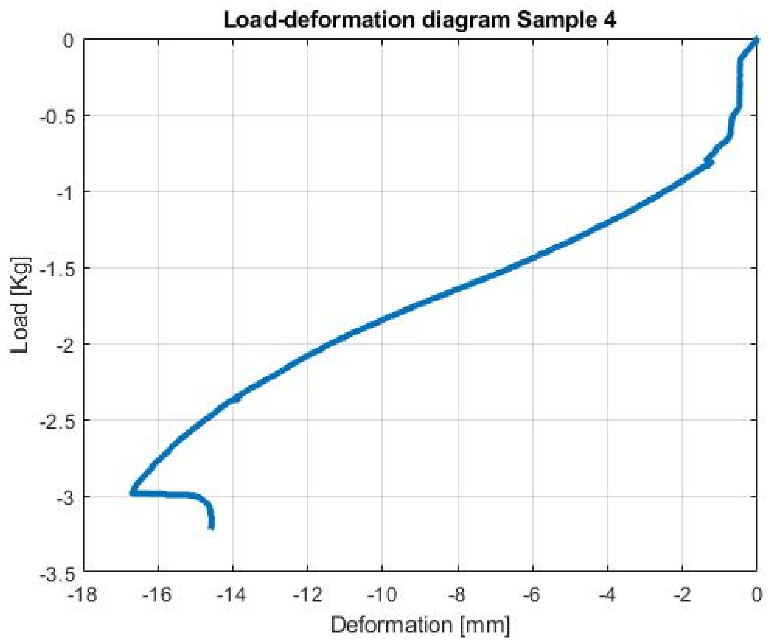

Figure 4.13: Load-deformation diagram for samples 4

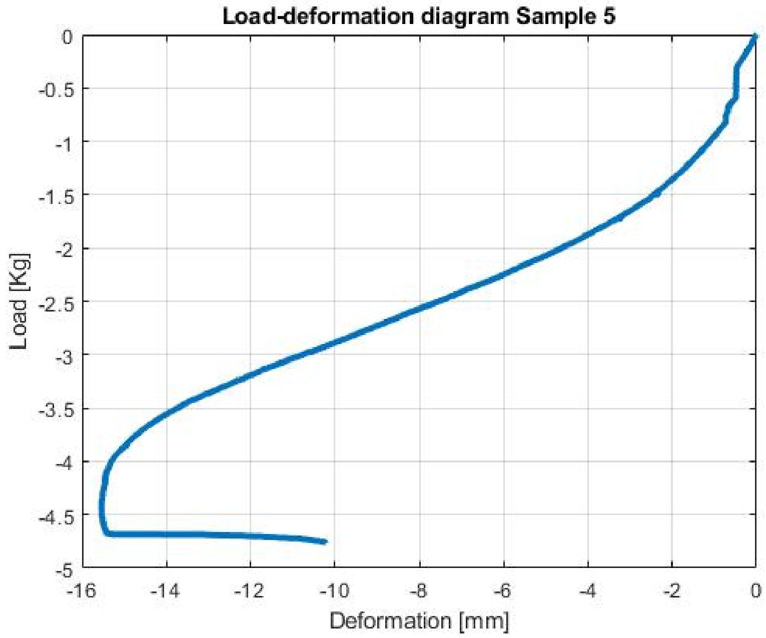

Figure 4.14: Load-deformation diagram for samples 5

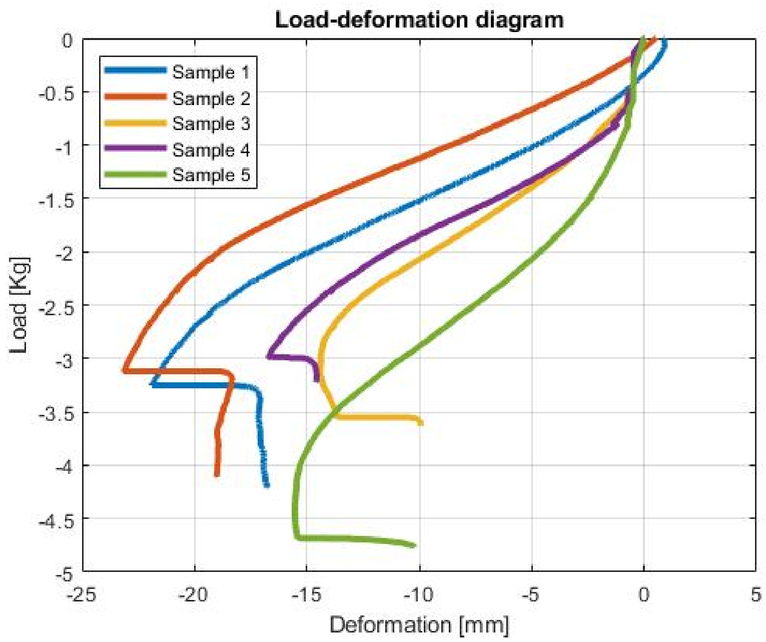

Figure 4.15: Load-deformation diagram for samples 3,4,5

As previously done, the equivalent stiffness has been evaluated through the knowledge of the angular coefficient, in figure 4.16 is shown, as an example, the analysis carried out on sample 3, while in tables 4.6, 4.7 the obtained results are shown (Calculated average value of 0,583 $[Nm^2]$. In addition, here again $GA*$ was neglected. In order to evaluate the influence of the sandwich core, equation 4.11

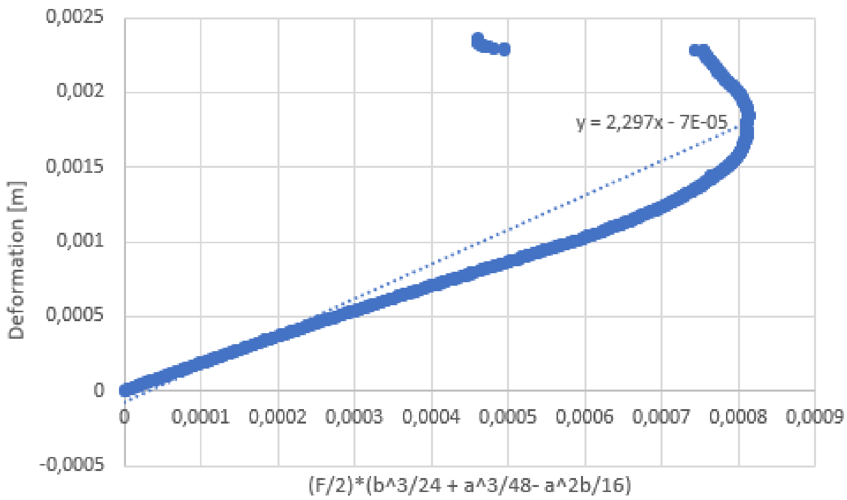

Figure 4.16: Analysis of the Equivalent stiffness of the third sample

has been reformulated, underlining the link between the effective stiffness and the previously calculated equivalent stiffness:

$$EI = \frac{\frac{F}{2}\left(\frac{b^3}{24} + \frac{a^3}{48} - \frac{a^2 b}{16}\right)}{w}(1+\alpha) \tag{4.13}$$

From which:

$$\alpha = 0{,}1843 \tag{4.14}$$

Consequently, the theoretical value has been revalued taking into account the α coefficient from which:

$$EI = \frac{0.685}{1+\alpha} = 0{,}578; \tag{4.15}$$

While in the case of flexible part:

$$\alpha = 0{,}000622 \tag{4.16}$$

The previous values of α have been estimated with respect to the theoretical value, therefore it is possible to notice that in the flexible case the contribution of the core is much lower and much more negligible than in the rigid case. It is now possible to enter the values for the test case, from which it can be noted that, in the rigid case:

$$\alpha = 0{,}1568; \tag{4.17}$$

while in the flexible case:

$$\alpha = 0{,}00097 \tag{4.18}$$

It is possible to observe how the value of alpha in the theoretical and experimental case are slightly different and this can derive from the structure of the core that presents inside empty spaces that are not detectable using the theoretical formulation.

Test Sample	Equivalent Stiffness Nm^2
Nr.1	0,541
Nr.2	0,5531
Nr.3	0,4353
Nr.4	1,006
Nr.5	0,3796
average value	0,583
theoretical value	0,578

Table 4.6: Equivalent Stiffness of the five samples (rigid part)

Test Sample	error %|
Nr.1	7,76
Nr.2	5,41
Nr.3	32,6
Nr.4	42.94
Nr.5	53.58

Table 4.7: Relative error of test-piece Equivalent stiffness (rigid part)

4.5 FEM Analysis

The FEM analysis was carried out with the help of the ANSYS software, which allowed the evaluation of the deformation of the samples (Fig. 4.17). The analysis was carried out first on the flexible part and then on the rigid part. The model used was made in such a way as to represent as much as possible the size of the piece, also for the mesh were used elements of type QUAD4 (1,3 mm) for the skins, while the elements of type HEX (1 mm) for the core (Fig.4.19, 4.18).

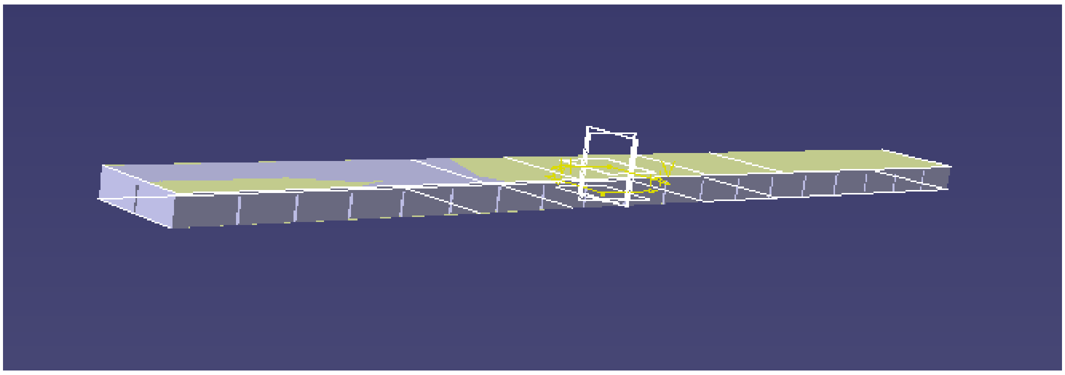

Figure 4.17: Geometry of the specimen

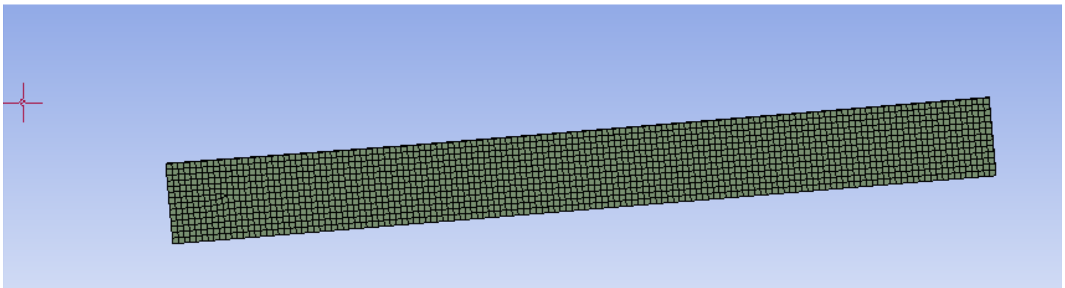

Figure 4.18: face mesh

4.5.1 Flexible part

For this part the support constraint has been inserted on the rigid part while on the flexible part the forces have been inserted. The analysis launched is of linear static type and the analyses have been set so as to know at each step the deformation as a function of the applied load. Figure 4.20 shows an example of the deformation obtained after the application of a force equal to 1 N. While in the Figure 4.21 is present a comparison between the experimental data and the obtained data

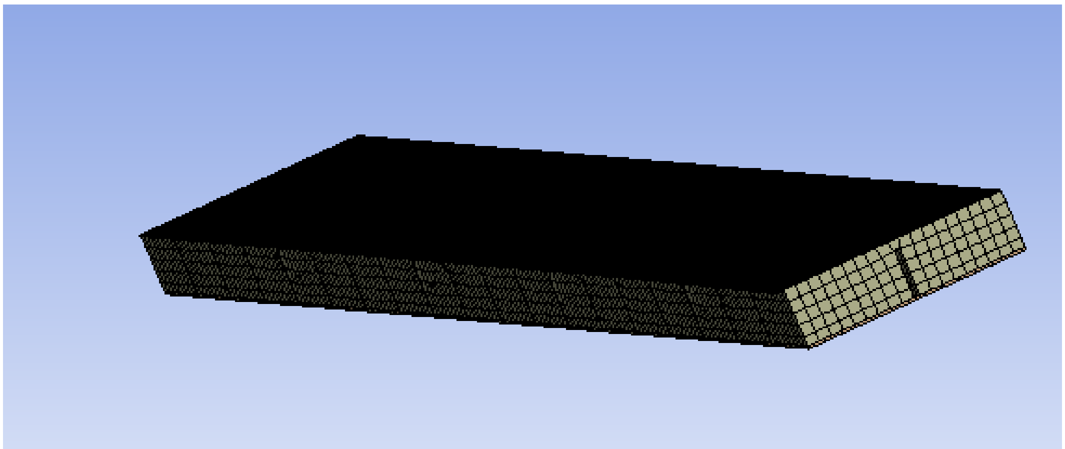

Figure 4.19: face core

through the fem analysis.
While the table 4.8 presents the main data used for fem analysis Using the graph

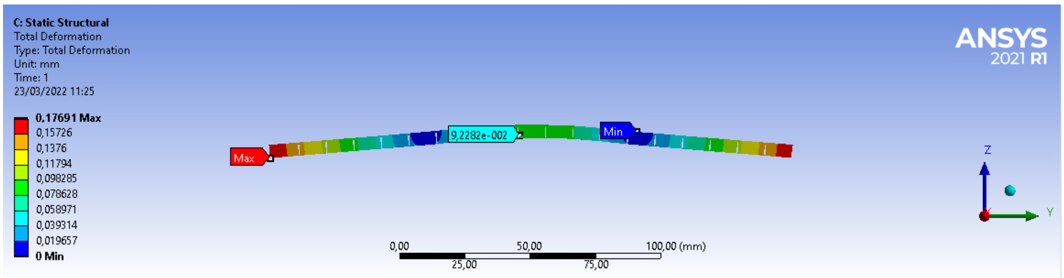

Figure 4.20: Deformation of the specimen after application of a force equal to 1 N

4.21 a comparison between the various data was made, in fact it was possible to calculate the average curve and the relative error was evaluated again.
Note how the relative error (In particular, an average curve was evaluated and the difference between the case curve and the average curve compared to the first) of all curves is in the around 2-3% unlike the 4 test piece which has a high deviation of about 19,6 %. While the data from the FEM analysis show a deviation from the average value of about 18%, this may result from several phenomena that have not been taken into account in the analysis, In fact, the compliance of the constraint that may introduce differences between the FEM and experimental analysis has not been taken into account, and a perfect adhesion between the layers has been hypothesized.

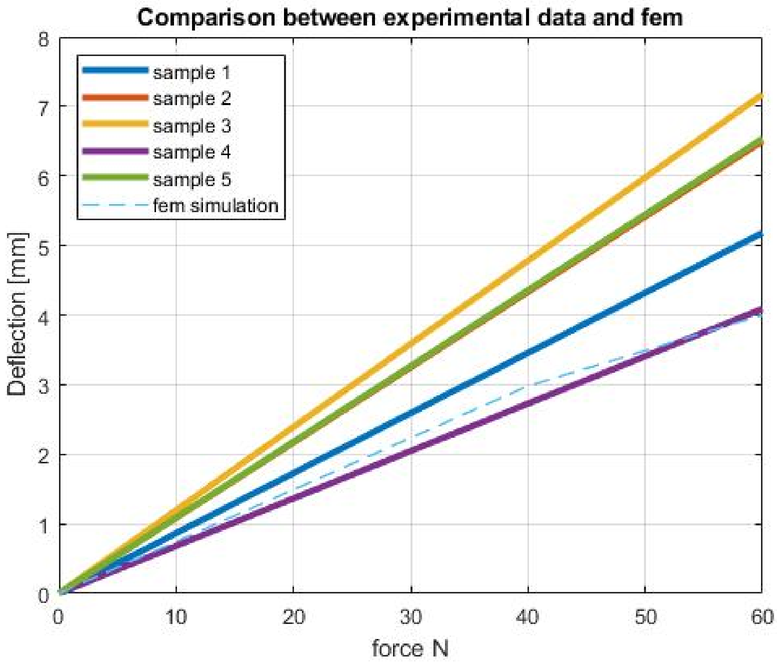

Figure 4.21: Comparison between experimental results and FEM analysis (flexible part)

Geometric data	Value
Beam length	200 mm
Beam width	19 mm
Core thickness	5 mm
Thick upper face	0,23 mm
Lower face thickness	0,23 mm
Material data	
Young module of the core	189 MPa
Young module of the upper face	120 GPa
Young module of the lower face	6 GPa
Data related to constraints and loads	
Distance between the application of the two loads	35 mm
Distance of application point of support and beam start	80 mm

Table 4.8: FEM data

4.5.2 Rigid part

Even in the rigid case it is possible to carry out the same evaluations described above. Consequently in Figure 4.22 the deformation of the specimen is shown following the application of 1 N, while in the Figure 4.23 a comparison between the experimental data and the FEM analysis is inserted. The relative error is

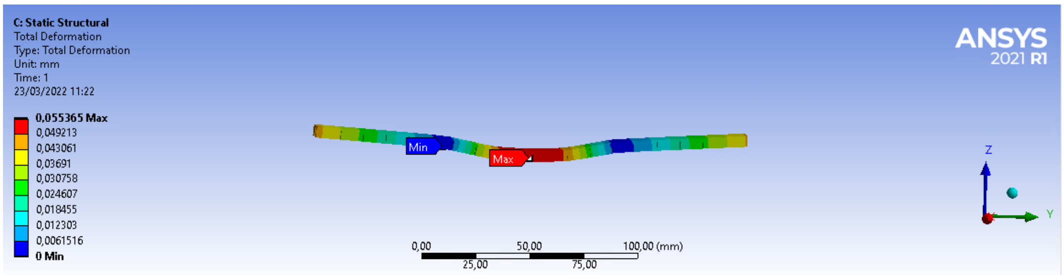

Figure 4.22: Deformation of the specimen after application of a force equal to 1 N

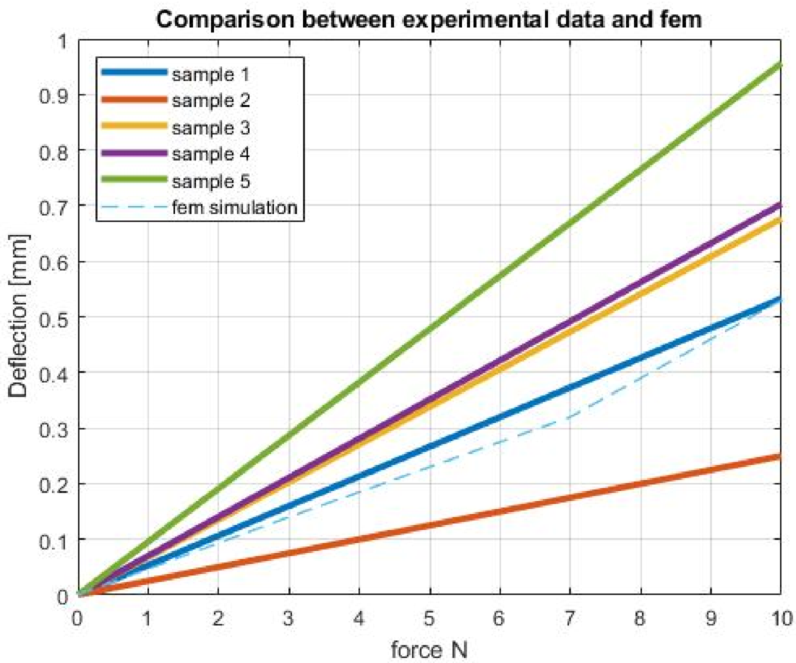

Figure 4.23: Comparison between experimental results and FEM analysis (rigid part)

$2-3\%$ while the fem is away from the average calculated value of about 3.84%.

The maximum deviation is 26.36%. Finally, also in the case of FEM analyses, the bending Equivalent stiffness was evaluated both in the rigid and flexible case and the results are shown in the table 4.9.

	Flexible part	Rigid part
Theoretical formulation [Nm^2]	0,0026	0,578
Experimental analysis [Nm^2] (Equivalent Stiffness)	0,003711	0,583
FEM [Nm^2]	0,00827	0,5899

Table 4.9: Comparison of the various data obtained in the previous sections for the rigid and flexible part

As can be seen from the table 4.9, the value of FEM is higher than in the other cases, and this may result from different phenomena. First of all in the theoretical case, for the flexible part, it has been hypothesized that the only layer that worked in compression was the rigid one, while inside the FEM the material in its entirety has been considered. Moreover, a perfect support and a perfect adhesion between the various layers has been suggested.
Finally, as can be seen from the graphs in the figures 4.23 and 4.9, it can be seen that the curve relative to FEM undergoes a slight variation of slope, and this can derive from the internal structure of the core that has empty spaces and this can cause local padding on the piece. In addition, applying equation 4.13 to the results obtained by FEM shows that, in the rigid case, the contribution of the core is equal to:

$$\alpha = 0{,}1586 \tag{4.19}$$

While in the flexible part:

$$\alpha = 0{,}0022 \tag{4.20}$$

Chapter 5

Gamma rays radiation test

Once the test was carried out to evaluate the flexural stiffness of the material, it was considered appropriate to proceed with an aging process carried out by the company Gammatom.srl. The process was conducted considering a dosage of 5 kGy [24] resulting from the dosage recorded on the MIR station (about 50 Gy in almost a year).
From the figure 5.1 we can see that in reality there is no visible visual difference between the aged and not, and it was, as a result, A further 4-point bending test shall be conducted to reveal any degradation of the flexural properties of the material.

Figure 5.1: Comparison between the sample subject to an aging process and the original specimen

5.1 Flexible part

Below are the main test results on the flexible part (Fig.5.2, 5.3, 5.4, 5.5, 5.6, 5.7).

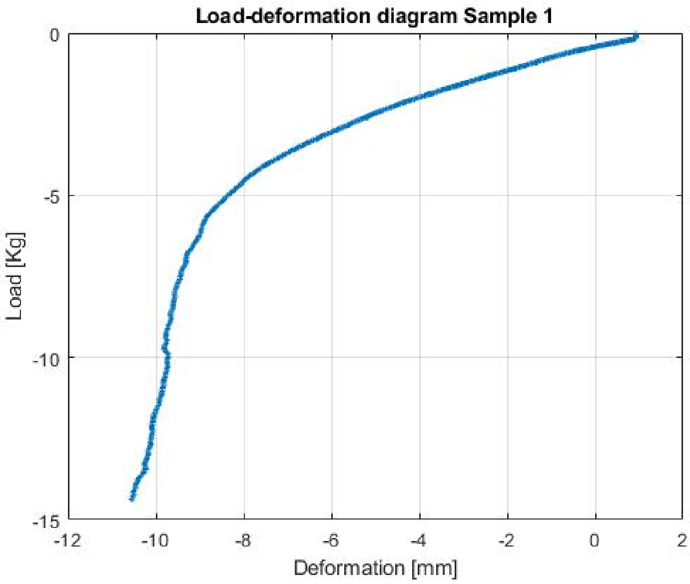

Figure 5.2: Load-deformation diagram for sample 1

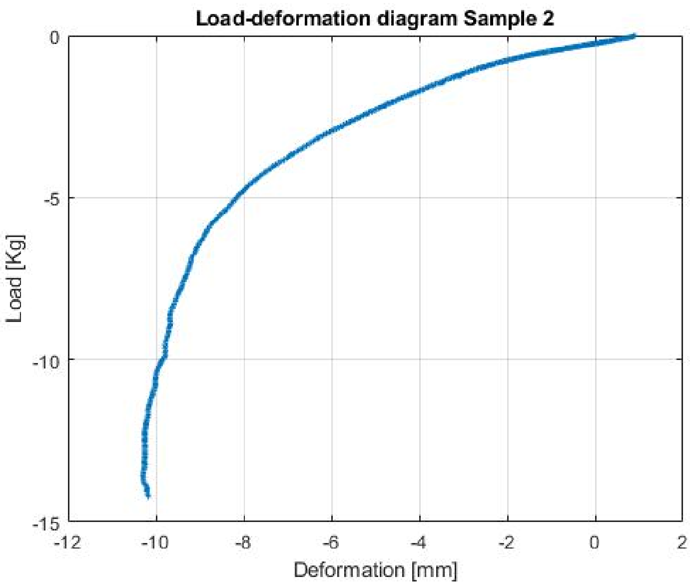

Figure 5.3: Load-deformation diagram for sample 2

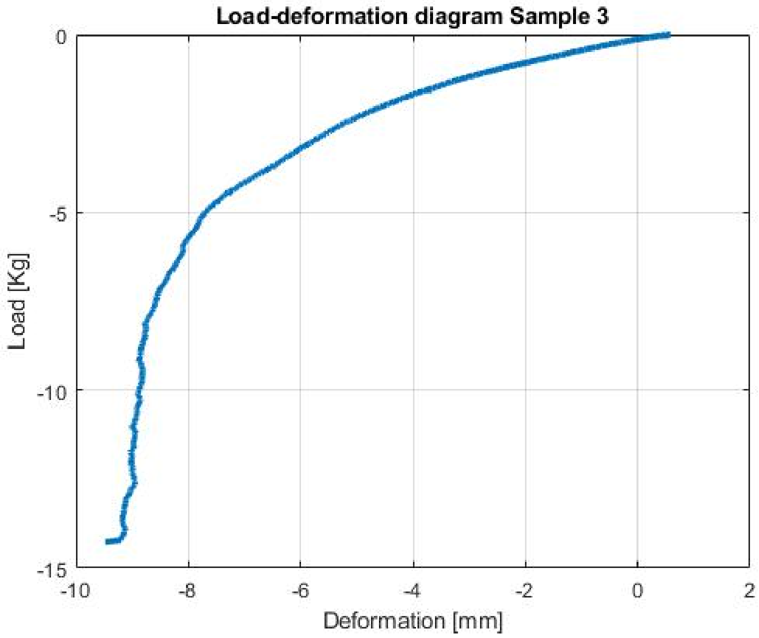

Figure 5.4: Load-deformation diagram for sample 3

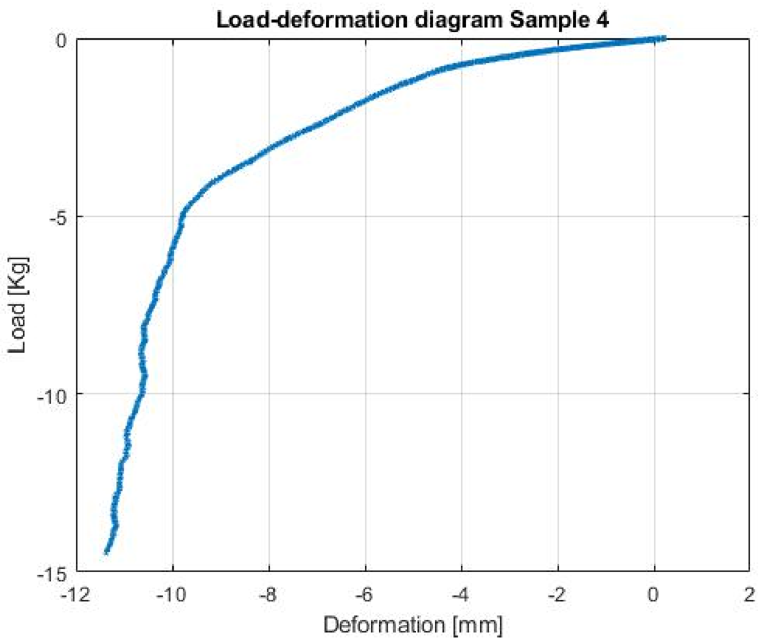

Figure 5.5: Load-deformation diagram for sample 4

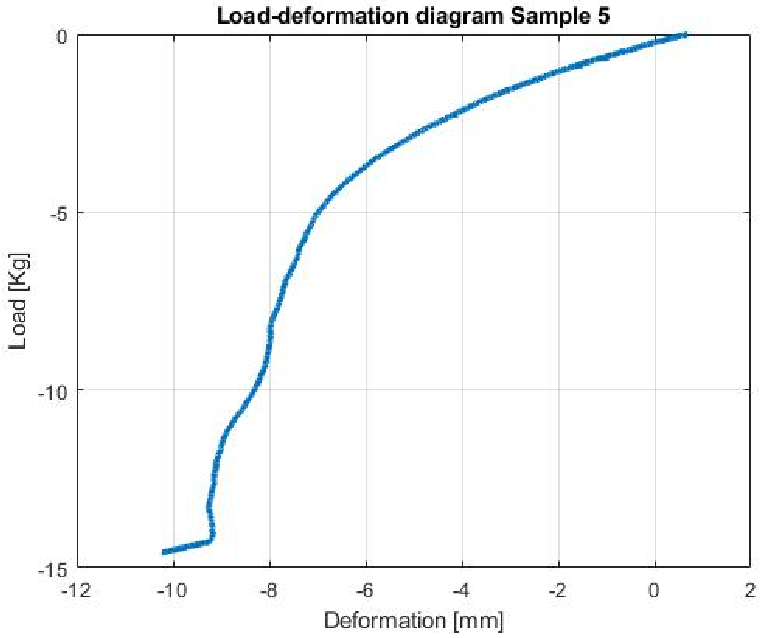

Figure 5.6: Load-deformation diagram for sample 5

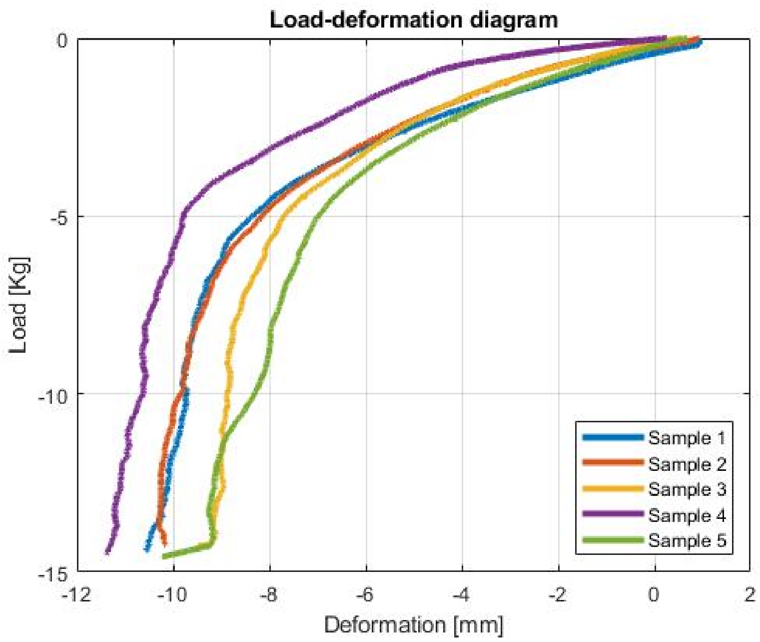

Figure 5.7: Load-deformation diagram for samples 1,2,3,4,5

At this point, the same analyses conducted previously have been carried out that have led to the results visible in the table 5.4:

Test Sample	Equivalent Stiffness Nm^2
Nr.1	0,006164
Nr.2	0,00326
Nr.3	0,008711
Nr.4	0,005757
Nr.5	0,004986
average value	0,00577

Table 5.1: Equivalent Stiffness of the five samples (flexible part)

From which in the table 5.2 the relative errors are visible, estimated like relationship between the difference of the real value regarding that estimated (average) on the real value.

Test Sample	error %|
Nr.1	6,31
Nr.2	77,1
Nr.3	33,7
Nr.4	0,31
Nr.5	15,84

Table 5.2: Relative error of bending Equivalent stiffness of aged specimens (flexible part)

When comparing the data of the aged specimens with those that did not undergo the same procedure, it can be seen that the values are similar to each other, therefore it can be inferred that no actual degradation of the material has occurred. However, the bending stiffness values of the aged specimens are higher and this may be due to the different test conditions that led to a difference in the result 5.3.

Test Sample	Equivalent Stiffness (no aging) Nm^2	Equivalent Stiffness (aging) Nm^2
Nr.1	0,003192	0,006164
Nr.2	0,003641	0,00326
Nr.3	0,004475	0,008711
Nr.4	0,003613	0,005757
Nr.5	0,003639	0,004986
average value	0,003711	0,00577

Table 5.3: Equivalent Flexural stiffness difference between aged and non-aged specimens (flexible part)

5.2 Rigid part

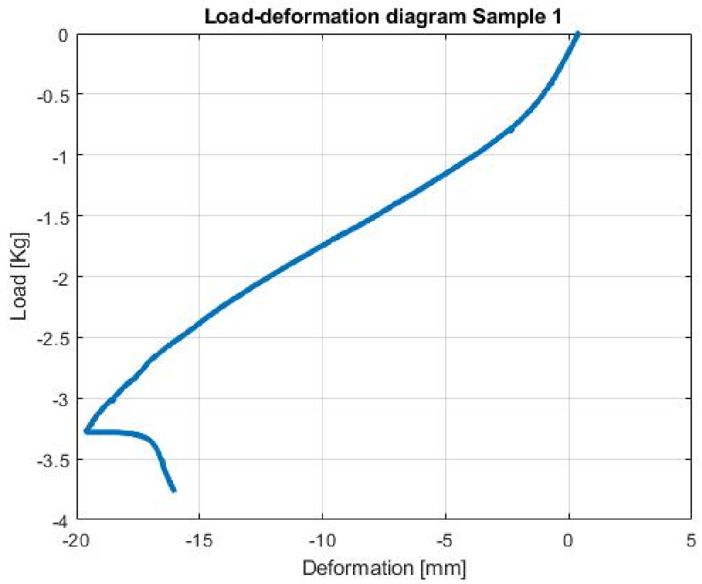

Figure 5.8: Load-deformation diagram for sample 1

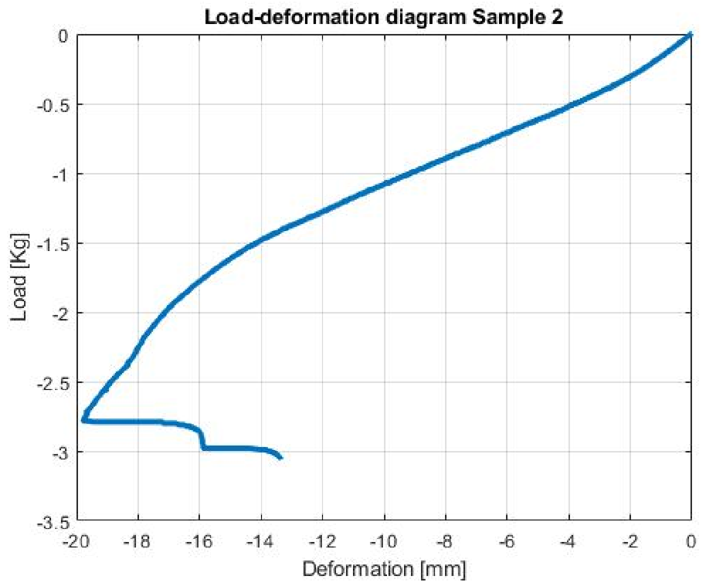

Figure 5.9: Load-deformation diagram for sample 2

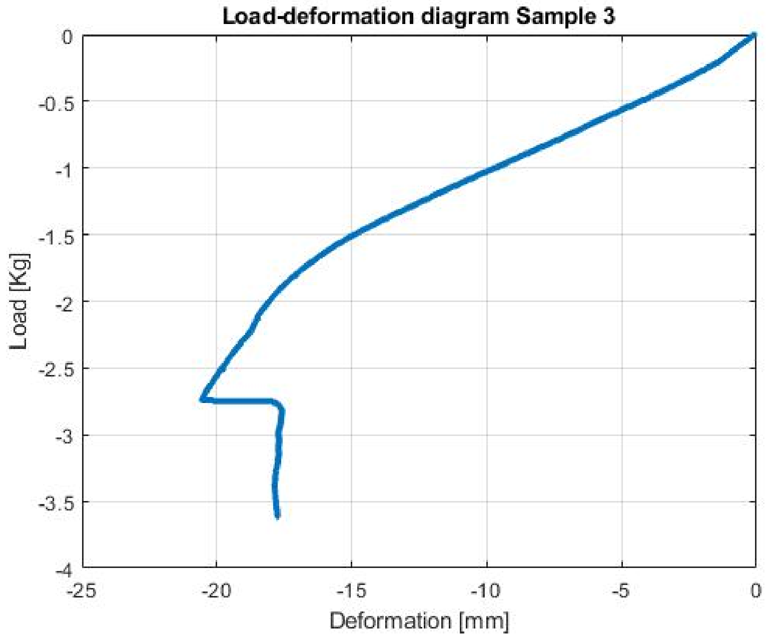

Figure 5.10: Load-deformation diagram for sample 3

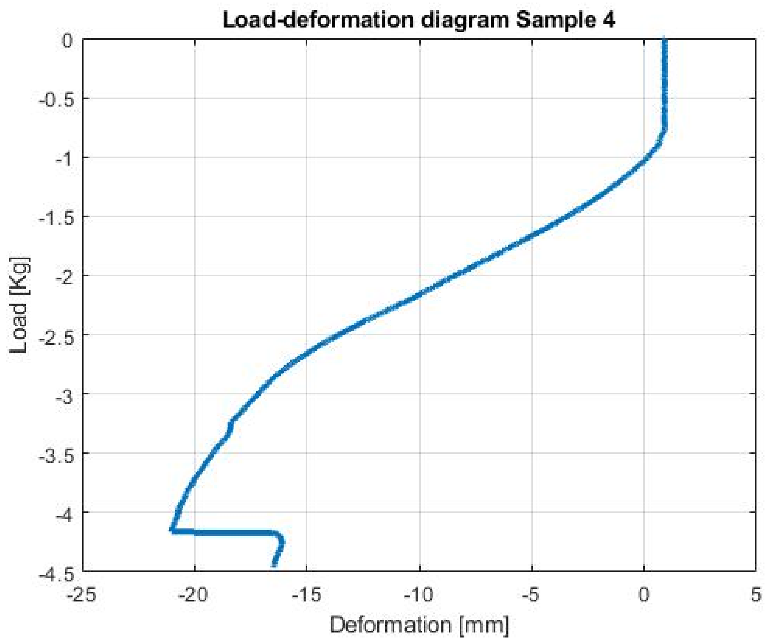

Figure 5.11: Load-deformation diagram for sample 4

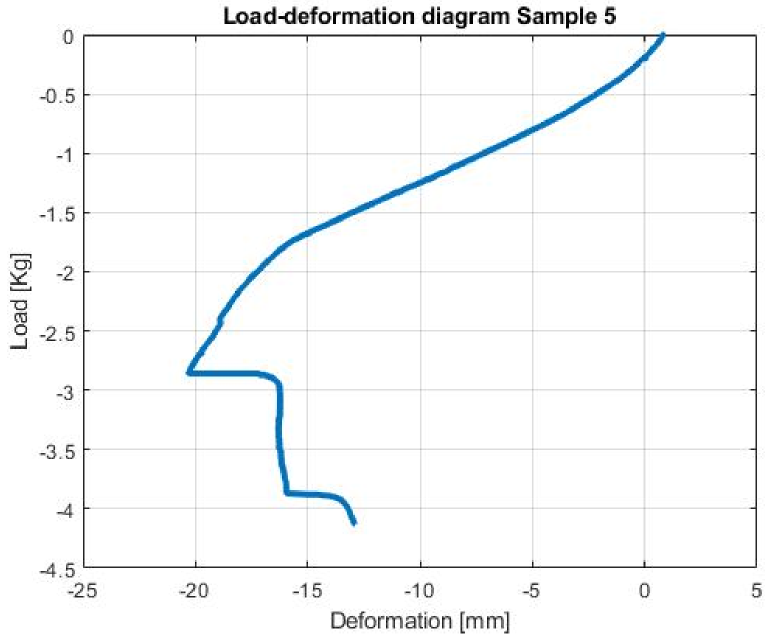

Figure 5.12: Load-deformation diagram for sample 5

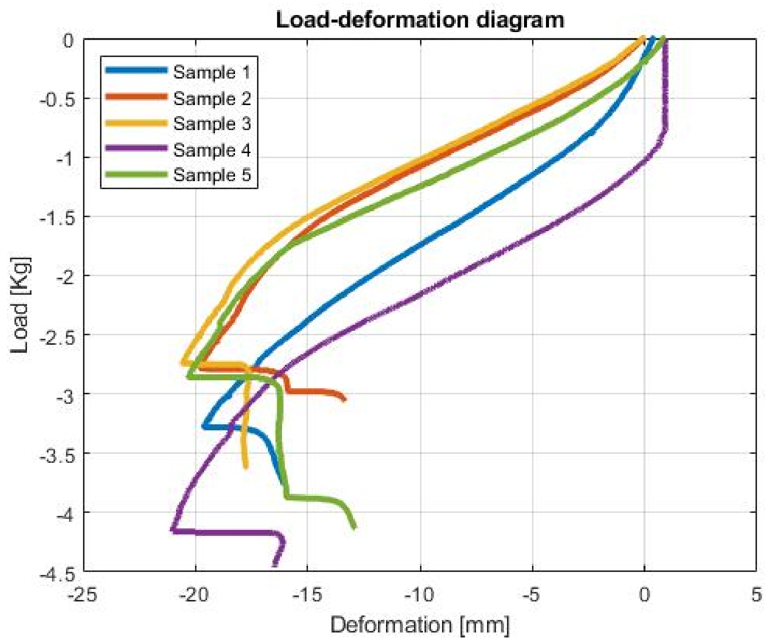

Figure 5.13: Load-deformation diagram for samples 1,2,3,4,5

Again, the results obtained in terms of flexural stiffness have been summarized in the table 5.4.

Test Sample	Equivalent Stiffness Nm^2
Nr.1	0,5065
Nr.2	0,5966
Nr.3	0,8710
Nr.4	0,5662
Nr.5	0,5394
average value	0,6159

Table 5.4: Equivalent Stiffness of the five samples (rigid part)

Test Sample	error %|
Nr.1	21,59
Nr.2	3,23
Nr.3	29,28
Nr.4	8,77
Nr.5	14,18

Table 5.5: Relative error of bending Equivalent stiffness of aged specimens (rigid part)

As previously done also in this case it is possible to insert a comparison table that highlights how even for the rigid part there were no degradation 5.6.

Test Sample	Equivalent Stiffness (no aging) Nmm^2	Equivalent Stiffness (aging) Nmm^2
Nr.1	0,541	0,5065
Nr.2	0,5531	0,5966
Nr.3	0,4353	0,8710
Nr.4	1,006	0,5662
Nr.5	0,3796	0,5394
average value	0,583	0,616

Table 5.6: Flexural Equivalent stiffness difference between aged and non-aged specimens (rigid part)

Chapter 6

Thermal Analysis

In order to better characterize the behavior of the material in a space environment, it was considered appropriate to perform a thermal analysis using the ANSYS software.
As a result, it was considered a LEO orbit and the heat flows that most affected the orbiting satellites in that belt were evaluated.

6.1 ANSYS Workbench

The thermal analysis was carried out with the help of ANSYS Workbench in which it carries out such analyses, in particular it evaluates the temperature distribution, taking into account the Fourier law, according to which the heat flow through a given surface is directly proportional to the thermal gradient and the thermal conductivity of the material.
Finally, a thermal balance is made:

$$[k(T)]\,\{T\} = \{Q\} \tag{6.1}$$

The software solves the problem through the matrix expression evaluating the contribution of each individual element. It is also assumed, in order to perform a stationary analysis, that the transient effects are negligible and both the thermal conductivity matrix ($[K]$) and the thermal load vector (Q) are either constant or temperature function.
In addition, various thermal loads can be defined within ANSYS: thermal load resulting from internal heat generation (can only be applied on solid bodies), perfect thermal insulation (is the condition for imposing a zero thermal power on the surface), heat flow (this type of load can only be applied to edges and surfaces) and finally thermal power (can be applied to both vertices and edges or to a whole

surface).
Once the thermal loads has been set the boundary conditions are the next step. It is possible to set as a condition a certain initial temperature (it is possible to do it both on the surfaces and on the bodies), the convection between the surfaces, and finally the irradiation. More specifically, convection can be defined by the following formulation:

$$q = hA(T_{sup} - T_e) \tag{6.2}$$

where h is a coefficient, A is the area of the surface while the contribution between brackets represents the difference between the surface temperature and the ambient temperature.
Irradiation, on the other hand, can be evaluated in the following way:

$$q = \sigma AF\epsilon(T_{sup}^4 - T_e^4) \tag{6.3}$$

Where, σ represents the constant of Stefan-Boltzman, F is the form factor (assumed to equal 1), while *Epsilon* is the emissivity of the body

6.2 Model Creation

The model used has the same geometric characteristics as shown in the previous chapters. For thermal analysis, moreover, the thermal conductivity coefficient has been defined taking an average value among those available on the market. From which they are obtained in visible values in the table 6.1.

Material	Coefficient of thermal conductivity $\frac{W}{mC}$
Prepreg Carbon	4,5
Rohacell (Foam)	0,03
Kevlar	0,3

Table 6.1: Thermal conductivity coefficients of the sandwich

In addition, a thermal flux on the upper surface of the material and an irradiation condition on the lower surface were applied to assess the temperature rise due to exposure in the Leo orbit. Specifically, in order to reproduce as closely as possible an operating condition, the thermal flux (Fig 6.1) [25] was evaluated under the worst possible conditions, taking into account the flow from the sun, the albedo and infrared radiation. Moreover in figure 6.2 it is possible to notice the direction and the intensity of the flow inserted for the numerical simulation on Ansys.

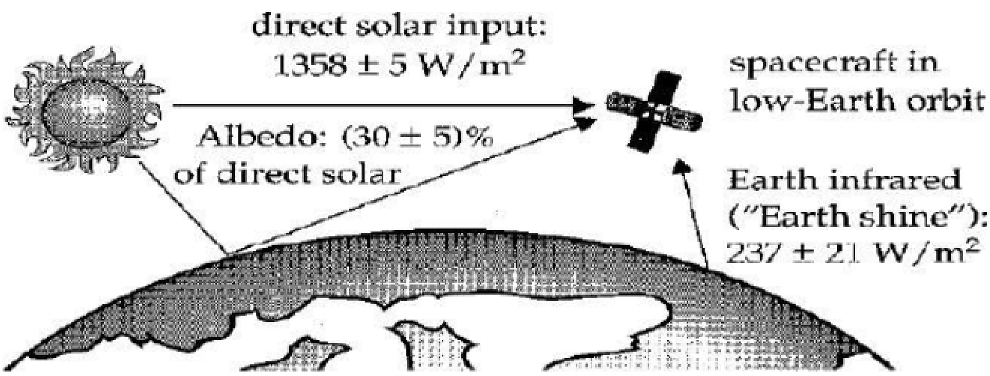

Figure 6.1: Thermal fluxes in LEO orbit

While the conditions of radiation was obtained taking into account an external temperature equal to that detectable on the ISS, or 121° [26].

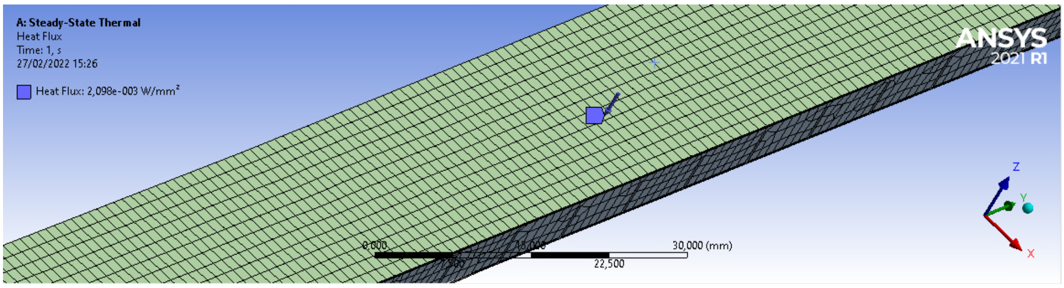

Figure 6.2: Ansys flow direction

6.3 Results

In order to evaluate the increase in temperature it was considered appropriate to proceed with a steady-state thermal analysis, which reported the result obtained in Fig 6.4. The obtained results show that the temperature reached, especially on the pre-impregnated carbon layer leads to serious problems on the materials, therefore a second analysis was carried out considering an aluminum foil placed as protection. In the table are shown the main coefficients of absorption of materials 6.2 [27].

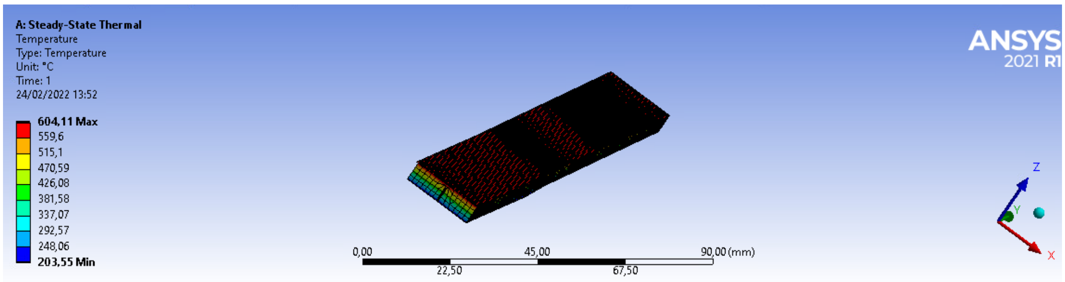

Figure 6.3: Results thermal analysis conducted without the aid of thermal protections

Material	Solar Absorption	Surface emissivity
Aluminum polished	0.09	0.03
Aluminum quarts overcoated	0.11	0.37
Aluminum foil	0.15	0.05
Aluminum anodized	0.14	0.84

Table 6.2: Main coefficients of absorption

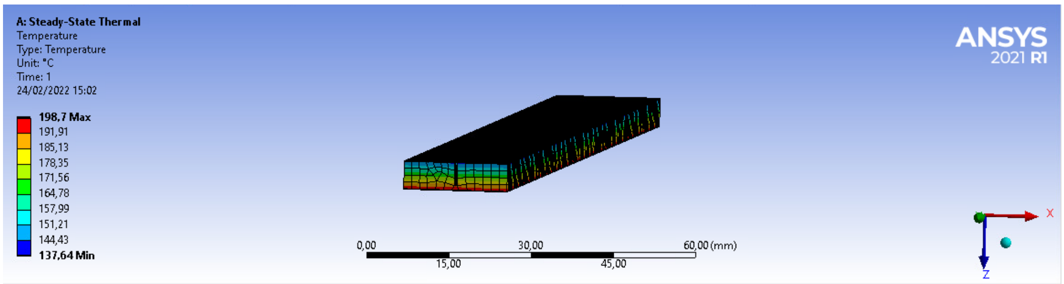

Figure 6.4: Results thermal analysis conducted with the aid of an Aluminum foil

From the figure you can see how the insertion of aluminum foil leads to a reduction of about 67.11%, making possible any exposure within the orbit LEO without damaging the material significantly. In addition, the trend of the temperature along the thickness is shown below (Fig. 6.5, 6.6, 6.7), both in the case where the thermal protection is present and in the absence of the latter.

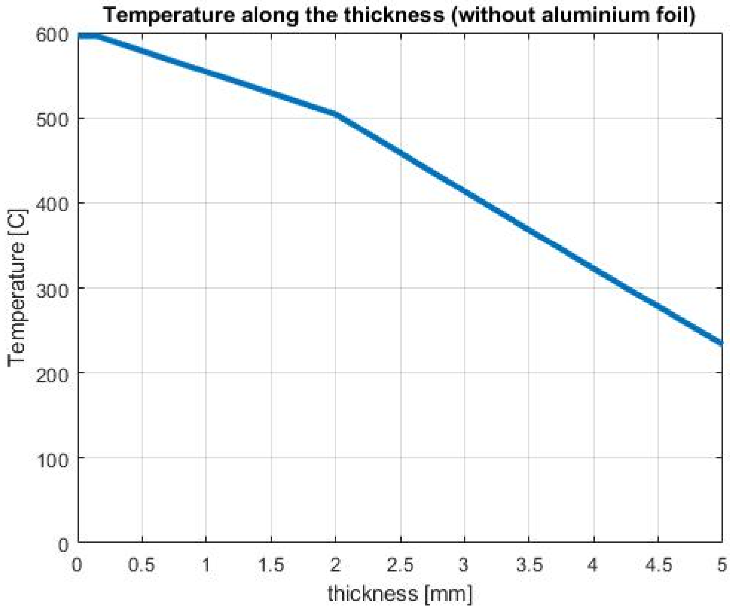

Figure 6.5: Temperature change along the thickness without the aluminum foil

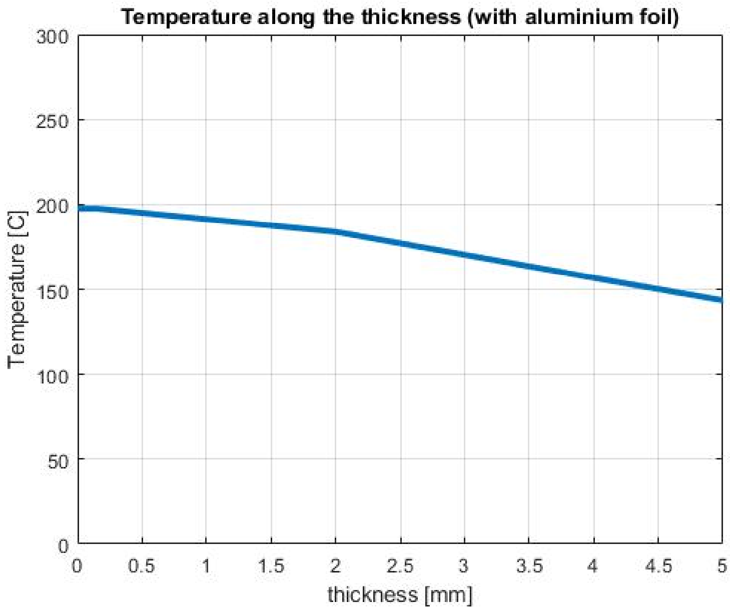

Figure 6.6: Temperature change along the thickness with the aluminum foil

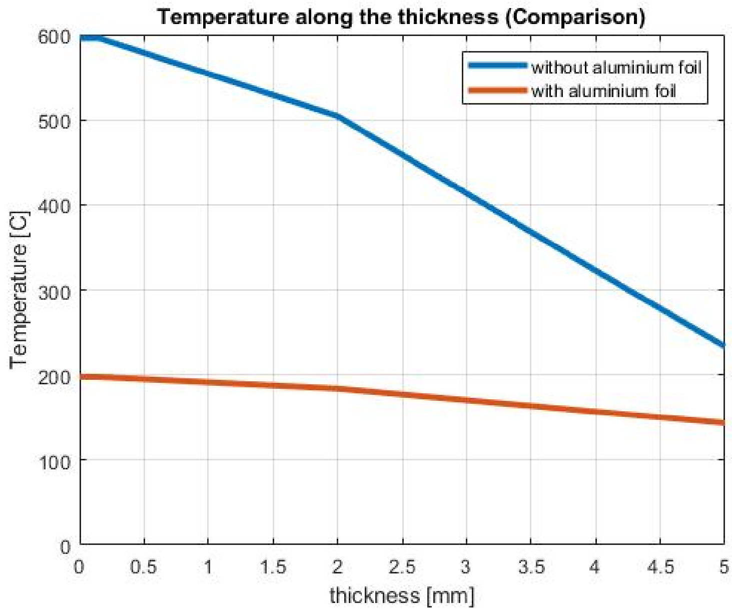

Figure 6.7: Comparison between the two cases analysed

Chapter 7

Conclusion

The main purpose of the thesis was to create a new configuration of material (developed by Composite Research) that could adapt to difficult space conditions. In addition to this, the main feature of being rollable on the one hand and flexible on the other had to be maintained. This then led to a four-point bending test, which was subsequently compared with the numerical data derived from the various theories analyzed above and the analysis carried out with the help of FEM.
Subsequently, the obtained values (assessed for both the flexible and rigid parts) were then compared with the values obtained from the same test considering the test pieces subject to aging from which it was discovered that the material, even if exposed to prolonged radiation, it does not undergo degradation.
Finally, a thermal analysis was conducted that showed how the material actually undergoes a sharp rise in temperature when subjected to thermal fluxes in the LEO orbit. Consequently, it was considered appropriate to assume an aluminum foil around the material, and this leads to a strong improvement in the results obtained.
After the analysis carried out it is possible to say that the hypothesized material has an excellent behaviour if exposed to the spatial environment because it keeps unchanged its bending behaviour despite the effect of radiation and thermal flows.
Finally, it can be stressed that, in order to fully analyse the characteristics of the material, it is essential to proceed with an outgassing test in order to use the material for space applications.

Bibliography

[1] Yugo Kimoto Jacob Kleiman Masahito Tagawa. *Protection of Materials and Structures From the Space Environment.* Vol. 1. JACOB I. KLEIMAN, ZELINA ISKANDEROVA, 2013 (cit. on pp. 1, 2, 5, 7–9, 12, 14, 15).

[2] P. Wurz. «Solar Wind Composition». In: *Proceedings of the 11th European Solar Physics Meeting "The Dynamic Sun: Challenges for Theory and Observations" (ESA SP-600), Leuven, Belgium* (2005), pp. 44.1–44.9 (cit. on pp. 3, 4).

[3] «Espulsioni di massa coronale». In: (). URL: `https://www.media.inaf.it/2017/05/09/espulsioni-massa-coronale/` (cit. on p. 4).

[4] Brian L. Diffey. «Sources and measurement of ultraviolet radiation». In: *Methods* 28.1 (2002), pp. 4–13. ISSN: 1046-2023. DOI: `https://doi.org/10.1016/S1046-2023(02)00204-9`. URL: `https://www.sciencedirect.com/science/article/pii/S1046202302002049` (cit. on p. 5).

[5] «The predicted growth of the low-Earth orbit space debris environment — an assessment of future risk for spacecraft». In: (). URL: `https://journals.sagepub.com/doi/10.1243/09544100JAERO192` (cit. on p. 6).

[6] «The atmosphere of Earth». In: (). URL: `https://www.britannica.com/place/Earth/The-atmosphere` (cit. on pp. 7, 8).

[7] Louis J. Lanzerotti Syun-Ichi Akasofu. «The Earth's magnetosphere». In: *Physics Today* (1975). URL: `https://physicstoday.scitation.org/doi/10.1063/1.3069238` (cit. on p. 8).

[8] R.A. Mewaldt. «Galactic cosmic ray composition and energy spectra». In: *Advances in Space Research* 14.10 (1994), pp. 737–747. ISSN: 0273-1177. DOI: `https://doi.org/10.1016/0273-1177(94)90536-3`. URL: `https://www.sciencedirect.com/science/article/pii/0273117794905363` (cit. on pp. 10, 11).

[9] «The atmospheres of other planets». In: (). URL: `https://www.britannica.com/science/atmosphere/The-atmospheres-of-other-planets` (cit. on pp. 12, 13).

[10] «Atomic oxygen». In: (). URL: https://www.reading.ac.uk/ir-spaceenvironment-atomicoxygen.aspx (cit. on p. 18).

[11] «ATOMIC OXYGEN EFFECTS ON MATERIALS». In: (1989). URL: https://ntrs.nasa.gov/citations/19890014169 (cit. on pp. 19–21).

[12] Bruce A. Banks, Kim K. de Groh, and Sharon K. Miller. «Low Earth Orbital Atomic Oxygen Interactions with Spacecraft Materials». In: *MRS Proceedings* 851 (2004), NN8.1. DOI: 10.1557/PROC-851-NN8.1 (cit. on p. 21).

[13] «Atomic oxygen resistant coatings for low earth orbit space structures.» In: *JOURNAL OF MATERIALS SCIENCE* 30 (1995), pp. 308–320 (cit. on pp. 21, 22).

[14] Zilong Jiao, Lixiang Jiang, Jipeng Sun, Jianguo Huang, and Yunfei Zhu. «Outgassing Environment of Spacecraft: An Overview». In: *IOP Conference Series: Materials Science and Engineering* 611.1 (Oct. 2019), p. 012071. DOI: 10.1088/1757-899x/611/1/012071. URL: https://doi.org/10.1088/1757-899x/611/1/012071 (cit. on pp. 22, 23).

[15] R.J. Elsey. «Outgassing of vacuum materials-II». In: *Vacuum* 25.8 (1975), pp. 347–361. ISSN: 0042-207X. DOI: https://doi.org/10.1016/0042-207X(75)91653-X. URL: https://www.sciencedirect.com/science/article/pii/0042207X7591653X (cit. on p. 24).

[16] «Standard Outgassing». In: (). URL: https://www.aac-research.at/outgassing/ (cit. on p. 24).

[17] Neil A. Walter and John J. Scialdone. «Outgassing Data for Selecting Spacecraft Materials». In: (June 1997) (cit. on p. 25).

[18] «NUCLEAR AND SPACE RADIATION EFFECTS ON MATERIALS». In: (June 1970) (cit. on pp. 26–30).

[19] «THERMAL EFFECTS ON MATERIALS». In: (). URL: http://webserver.dmt.upm.es/~isidoro/ot1/Thermal%5C%20effects%5C%20on%5C%20materials.pdf (cit. on p. 31).

[20] «Thermal Conductivity». In: (). URL: https://phys.libretexts.org/Bookshelves/Thermodynamics_and_Statistical_Mechanics/Book%5C%3A_Heat_and_Thermodynamics_(Tatum)/04%5C%3A_Thermal_Conduction/4.03%5C%3A_Thermal_Conductivity#:~:text=There%5C%20is%5C%20a%5C%20temperature%5C%20gradient,heat%5C%20is%5C%20flowing%5C%20down%5C%20it).&text=The%5C%20ratio%5C%20of%5C%20the%5C%20rate,symbol%5C%20K%5C%20for%5C%20thermal%5C%20conductivity (cit. on p. 31).

[21] H K M Al-Jothery, T M B Albarody, P S M Yusoff, M A Abdullah, and A R Hussein. «A review of ultra-high temperature materials for thermal protection system». In: *IOP Conference Series: Materials Science and Engineering* 863.1 (May 2020), p. 012003. DOI: 10.1088/1757-899x/863/1/012003. URL: https://doi.org/10.1088/1757-899x/863/1/012003 (cit. on pp. 32, 33).

[22] Allen H.G. «Analysis and Design of Structural Sandwich Panels». In: Pergamon Press, Oxford, 1969 (cit. on p. 40).

[23] «ASTM D7250/D7250M Standard Practice for Determining Sandwich Beam Flexural and Shear Stiffness». In: () (cit. on p. 49).

[24] W. Schöner, Michael Hajek, M. Noll, Rita Ebner, Norbert Vana, Manfred Fugger, Y. Akatov, Vyacheslav Shurshakov, and V. Arkhangelsky. «MEASUREMENT OF THE DEPTH DOSE AND LET DISTRIBUTION AT THE SURFACE AND INSIDE OF SPACE STATION MIR». In: (Jan. 1999) (cit. on p. 69).

[25] Ceren Cansu Guvenc, Batuhan Topcu, and Ceyhun Tola. «Mechanical Design and Finite Element Analysis of a 3 Unit Cubesat Structure». In: June 2018 (cit. on p. 80).

[26] «How Difficult Is It To Keep The Space Station Warm?» In: (). URL: https://www.forbes.com/sites/quora/2018/10/24/how-difficult-is-it-to-keep-the-space-station-warm/?sh=274067374af7 (cit. on p. 81).

[27] «Heliostat Design Concepts.» In: (). URL: http://www.redrok.com/concept.htm#emissivity (cit. on p. 81).

Ringraziamenti

Desidero ringraziare il Professore Giacomo Frulla, relatore di questa tesi, per il supporto e la disponibilità mostrata negli ultimi mesi. Vorrei inoltre ringraziare l'ingegnere Nicola Giulietti per avermi dato la possibilità di svolgere questa tesi in collaborazione con la Composite Research e per il sostegno durante lo svolgimento delle attività. Vorrei ringraziare, inoltre, la mia famiglia per avermi supportato e soprattutto sopportato durante questi anni complicati. Infine mi piacerebbe ringraziare Angelica, Antonio e Stefania, principali compagni e sostenitori di questa avventura.